

# Multiple locations of near-infrared coronal lines in NGC 5548

Daniel Kynoch<sup>1</sup>,<sup>1,2</sup>★†, Hermine Landt,<sup>2</sup>★†, Maryam Dehghanian,<sup>3</sup> Martin J. Ward<sup>2</sup>† and Gary J. Ferland<sup>3</sup>

<sup>1</sup>*Astronomical Institute, Czech Academy of Sciences, Boční II 1401, 141 00 Prague, Czech Republic*

<sup>2</sup>*Centre for Extragalactic Astronomy, Department of Physics, Durham University, South Road, Durham, DH1 3LE, UK*

<sup>3</sup>*Department of Physics and Astronomy, University of Kentucky, Lexington, KY 40506, USA*

Accepted 2022 August 25. Received 2022 August 25; in original form 2022 March 18

## ABSTRACT

We present the first intensive study of the variability of the near-infrared coronal lines in an active galactic nucleus (AGN). We use data from a 1-yr-long spectroscopic monitoring campaign with roughly weekly cadence on NGC 5548 to study the variability in both emission line fluxes and profile shapes. We find that in common with many AGN coronal lines, those studied here are both broader than the low-ionization forbidden lines and blueshifted relative to them, with a stratification that implies an origin in an outflow interior to the standard narrow line region. We observe for the first time [S VIII] and [Si VI] coronal line profiles that exhibit broad wings in addition to narrow cores, features not seen in either [S IX] or [Si X]. These wings are highly variable, whereas the cores show negligible changes. The differences in both the profile shapes and variability properties of the different line components indicate that there are at least two coronal line regions in AGN. We associate the variable, broad wings with the base of an X-ray heated wind evaporated from the inner edge of the dusty torus. The coronal line cores may be formed at several locations interior to the narrow line region: either along this accelerating, clumpy wind or in the much more compact outflow identified with the obscurer and so emerging on scales similar to the outer accretion disc and broad-line region.

**Key words:** galaxies: active – galaxies: Seyfert – quasars: emission lines – quasars: individual: NGC 5548 – infrared: galaxies.

## 1 INTRODUCTION

Active galactic nuclei (AGN) display emission lines from both permitted and forbidden transitions. The latter are usually associated with the narrow emission line region (NLR), which is formed by gas of low densities ( $\log [n_{\text{H}}/\text{cm}^{-3}] \sim 3\text{--}6$ ) located at relatively large distances from the central ionizing source (from a few pc up to several 100 pc). But some of these forbidden emission lines require energies  $\gtrsim 100$  eV to form the corresponding ions, have higher critical densities for collisional deexcitation ( $\log [n_{\text{e}}^{\text{crit}}/\text{cm}^{-3}] \sim 7\text{--}10$ ) and broader profiles (full widths at half-maxima [FWHM]  $\sim 500\text{--}1500$  km s<sup>-1</sup>) than the low-ionization narrow emission lines (e.g. Penston et al. 1984; Appenzeller & Oestreich 1988; Giannuzzo, Rieke & Rieke 1995; Erkens, Appenzeller & Wagner 1997; Rodríguez-Ardila et al. 2002, 2011): these are the so-called ‘coronal lines’, named after their presence in the spectrum of the solar corona (Oke & Sargent 1968). Coronal lines are forbidden fine-structure transitions arising from highly ionized states of heavy metals. Low-energy electrons or weak interactions with high-energy electrons can efficiently excite these transitions from the ground state; however, the formation of the ions themselves requires relatively high energies.

Both types of AGN display coronal lines (Osterbrock 1977; Koski 1978), but they are stronger in broad-line (type 1) than in narrow-line (type 2) AGN relative to their low-ionization narrow emission lines

(Murayama & Taniguchi 1998). Therefore, it is likely that the coronal line region has two components, one compact and one spatially extended, with only the latter remaining unobscured by the dusty torus in type 2 AGN. Support for this assumption comes from the fact that the emission from this region is often extended but much less so than that from the low-ionization NLR (on scales of  $\sim 80\text{--}150$  pc; e.g. Prieto, Marco & Gallimore 2005; Müller Sánchez et al. 2006; Müller-Sánchez et al. 2011; Mazzalay et al. 2013; Riffel et al. 2021; although Negus et al. 2021 have recently reported coronal line emission on kpc scales). Furthermore, coronal lines are often blueshifted relative to the low-ionization narrow lines (e.g. Penston et al. 1984; Erkens et al. 1997; Rodríguez-Ardila et al. 2002), which indicates an outflowing wind component. Given their similar physical conditions, it could be that the partly ionized gas that produces absorption lines and edges in the soft X-ray spectra of AGN, i.e. the so-called ‘warm absorber’, also produces the coronal lines in its (colder) outer regions (Netzer 1993; Erkens et al. 1997; Porquet et al. 1999). In any case, the coronal line region is most likely dust free since strong emission from refractory elements such as iron, silicon, and calcium are observed, which would be severely reduced in a dusty environment (Ferguson, Korista & Ferland 1997).

The high ionization potentials ( $\chi$ ) required for the coronal lines can be found either in a hot, collisionally ionized plasma or be produced by the hard continuum in AGN if the gas is photoionized. In the first case, the electron temperatures would be of the order of  $\log (T_{\text{e}}/\text{K}) \approx 6$  and in the second case much lower ( $\log [T_{\text{e}}/\text{K}] \sim 4\text{--}5$ ). Currently, photoionization is favoured, since for most AGN the observed flux ratios between different coronal lines can be reproduced within a factor of  $\sim 2\text{--}3$  by these models (Oliva et al. 1994; Ferguson et al. 1997; Landt et al. 2015a, b), whereas in the case of a hot plasma,

\* E-mail: d.kynoch@soton.ac.uk (DK); hermine.landt@durham.ac.uk (HL)

† Visiting Astronomer at the Infrared Telescope Facility, which is operated by the University of Hawaii under contract NNH14CK55B with the National Aeronautics and Space Administration (NASA).

either its temperature needs to be fine-tuned within a very narrow range (Oliva et al. 1994) or no acceptable fit can be obtained (Landt et al. 2015a, b).

More recently, growing interest in near-IR coronal lines has arisen due to their potential for yielding estimates of the black hole mass in AGN (Cann et al. 2018; Rodríguez-Ardila et al. 2020). Since these coronal lines can potentially probe the accretion disc spectral energy distribution (SED) at far-UV/soft-X-ray energies, a regime difficult to observe but most influenced by the mass of the black hole, they could uncover the long-sought population of intermediate mass black holes, which are crucial for our understanding of black hole growth over cosmic time (Hopkins et al. 2012). Even more importantly, if near-IR coronal lines can help identify AGN in dwarf galaxies in large numbers (Bohn et al. 2021; Cann et al. 2021), it would open up a unique opportunity to understand the role of AGN feedback in galaxy evolution and to test cosmological models. Since dwarf galaxies are believed to be dark matter-dominated, these sources serve as important probes in the low-mass halo regime, in particular for the Lambda Cold Dark Matter ( $\Lambda$ CDM) paradigm (Navarro 2019).

Variability studies can strongly constrain the properties of the coronal line region, in particular, if several lines can be studied simultaneously and together with other AGN components such as the broad emission line region (BLR) and the UV/X-ray continuum. However, since these emission lines are relatively weak and so require high-quality spectroscopy, very few studies of this kind have been attempted so far. Veilleux (1988) presented the only systematic study of coronal line variability. In a sample of  $\sim 20$  AGN, he found firm evidence that both the [Fe VII]  $\lambda 6087$  and [Fe X]  $\lambda 6375$  emission lines varied (during a period of a few years) for only one source (NGC 5548) and tentative evidence for another seven sources (including NGC 4151). Then, within a general optical variability campaign on Mrk 110 for about half a year, Kollatschny et al. (2001) reported strong [Fe X] variations. Strong variability of the coronal lines manifested mainly as a fading of the flux was first reported for IC 3599 (Brandt, Pounds & Fink 1995; Grupe et al. 1995) and is now usually associated with a new class of non-active galaxies, the so-called ‘strong coronal line emitters’ (or ‘coronal line forest AGN’). Most of these sources have been detected in the Sloan Digital Sky Survey (SDSS: York et al. 2000) and a stellar tidal disruption event seems to be the most plausible explanation for the strong fading of their coronal lines over a time period of several years (Komossa et al. 2008, 2009; Gelbord, Mullaney & Ward 2009; Wang et al. 2011, 2012; Yang et al. 2013; Rose, Elvis & Tadhunter 2015; Winkler 2016; Cerqueira-Campos et al. 2021; van Velzen et al. 2021).

Landt et al. (2015a, b) presented the first extensive studies of the coronal line variability in individual AGN. Their data sets for the nearby, well-known sources NGC 4151 and NGC 5548 included a handful of epochs of quasi-simultaneous optical, near-IR, and X-ray spectroscopy spanning a period of several years. They found very different variability behaviours for the two sources, with only weak variations detected for the coronal lines in NGC 4151, but strong flux variability (mainly a decrease) by factors of  $\sim 2$ – $4$  observed in NGC 5548. In both sources, the coronal line gas density was constrained to relatively low values of  $\log(n_e/\text{cm}^{-3}) \sim 3$  for a relatively high ionization parameter of  $\log U \sim 1$ , which put it at a distance from the central ionizing source of a few light-years and so well beyond the hot inner face of the obscuring dusty torus. Therefore, they proposed that the coronal line region in AGN is an independent entity rather than part of a continuous gas distribution connecting the BLR and low-ionization NLR, possibly an X-ray heated wind as first suggested by Pier & Voit (1995).

Here we revisit the variability of the near-IR coronal lines in NGC 5548 with a much-improved data set that allows us to study in detail both flux and profile shape variations. Our paper is structured as follows: In Section 2, we briefly discuss the near-IR spectroscopy, which we analyse in detail in Section 3. In Section 4, we present the results on the coronal line profiles and their variability, which we compare to theoretical photoionization simulations in Section 5. In Section 6, we discuss the likely origin of the near-IR coronal lines in NGC 5548. Finally, in Section 7, we present a summary of our main results and conclusions. We quote all laboratory line wavelengths as vacuum wavelengths and define velocities as negative if they are in the blue-shifted (outflowing) direction.

## 2 THE DATA

Landt et al. (2019) observed NGC 5548 between 2016 August and 2017 July with the SpeX spectrograph (Rayner et al. 2003) at the NASA Infrared Telescope Facility (IRTF), a 3-m telescope on Maunakea, Hawaii. The main aim of this near-IR spectroscopic reverberation mapping campaign was to measure the time delay of the hot dust in the obscuring torus together with estimates of the torus radius based on thermal equilibrium arguments. Another important goal was to study the variability of emission lines, such as those from the coronal line region.

The campaign achieved a total of 18 near-IR spectra with an average cadence of about ten days, excluding a 3.5-month period when the source was unobservable. They used the short cross-dispersed (SXD) mode (0.7–2.55  $\mu\text{m}$ ) and a  $0.3'' \times 15''$  slit oriented at the parallactic angle, resulting in an average spectral resolution of  $R = 2000$  or FWHM  $\sim 150 \text{ km s}^{-1}$ . The spectra have in general a relatively high signal-to-noise (S/N) ratio with an average continuum S/N  $\sim 100$ .

Care was taken to ensure *a posteriori* an accurate absolute flux calibration. As described in detail in Landt et al. (2019) (see their section 3.3), they used the narrow forbidden emission line [S III]  $\lambda 9531$  to align the flux scale of the spectra and verified it with a photometric light curve. Furthermore, the impact of the extended low-ionization emission line region on the enclosed flux in the slit was assessed based on a near-IR Integral Field Unit (IFU) observation. For our following analysis, we used the observed spectra with their multiplicative photometric correction factors applied. We estimated that the uncertainty on the wavelength calibrations of our spectra is on average  $0.15 \text{ \AA}$ , which corresponds to  $\approx 2$ – $5 \text{ km s}^{-1}$  at the location of the lines studied. We report velocity shifts of the coronal lines measured relative to the [S III]  $\lambda 9531$  narrow emission line, and the wavelength calibration uncertainty was added to the measurement uncertainties.

## 3 THE SPECTRAL ANALYSIS

The large wavelength range our cross-dispersed near-IR spectra covers four strong coronal lines in NGC 5548. Two of them are produced by highly ionized sulphur ([S VIII] and [S IX]) and two by highly ionized silicon ([Si VI] and [Si X]). We list their basic properties in Table 1. Our main aim was to reliably isolate the coronal lines in the individual spectra in order to measure their fluxes, velocity shifts, and profile shapes and study their variability. However, since coronal lines are in general weak emission lines, we analysed them first in the high-quality mean spectrum presented by Landt et al. (2019) and then used these results as a guide for our analysis of the individual spectra, which have a lower S/N in the wavelength regions of interest.

**Table 1.** Coronal emission lines and their contaminants.

Ion (1)	Coronal emission line			Contaminant emission line	
	$\lambda$ [ $\mu\text{m}$ ] (2)	$\chi$ [eV] (3)	$\log(n_e^{\text{crit}})$ [ $\text{cm}^{-3}$ ] (4)	Ion (5)	$\lambda$ [ $\mu\text{m}$ ] (6)
[S VIII]	0.9914	281.0	9.5	[C I] [C I] H I (Pa $\delta$ ) He II	0.9827 0.9853 1.005 1.0126
[S IX]	1.2523	328.8	9.4	Unknown [Fe II] Unknown H I (Pa $\beta$ )	1.248 1.2570 1.262 1.282
[Si X]	1.4305	351.1	8.1		
[Si VI]	1.9650	166.8	8.5	H I (Pa $\alpha$ ) H I (Br $\delta$ ) H <sub>2</sub>	1.875 1.9440 1.957

*Note.* The columns are: (1) Ion; (2) vacuum rest-frame wavelength; (3) ionization potential; and (4) critical density calculated with CLOUDY for the coronal emission lines at temperature  $\log(T_e/\text{K}) = 4$ ; (5) ion; and (6) vacuum rest-frame wavelength for the contaminating broad and narrow emission lines. The emission line parameters of all these lines are listed in Table 2.

We performed the emission line and continuum fits using custom Python scripts employing the package LMFIT (Newville et al. 2014), which is a non-linear, least-squares, curve-fitting routine based on the Levenberg–Marquardt algorithm. The majority of the emission lines can be adequately modelled with Gaussian profiles. From these fits, we have calculated the emission line fluxes and FWHMs and the associated uncertainties. All narrow emission lines were allowed to have widths varying in the range of  $\text{FWHM} = 100\text{--}900 \text{ km s}^{-1}$  and the widths of broad Gaussian components were allowed to vary in the range of  $1000\text{--}9999 \text{ km s}^{-1}$ . Values quoted for the FWHMs of the emission lines have been corrected for instrumental broadening. The velocity shifts of the near-IR lines are determined from the centroids of the fitted Gaussians and measured relative to the [S III]  $\lambda 9531$  line, which is assumed to have zero velocity shift. The uncertainties on the velocity shifts incorporate the uncertainty on the wavelength calibration of our spectra. More details on the fitting procedures for specific lines and blends are given in the following subsections.

### 3.1 The mean spectrum

Fig. 1 shows the wavelength regions around the four near-IR coronal lines in the mean spectrum. Out of these, only [Si X] is free from contaminating neighbouring emission lines, whereas the other coronal lines are located close to a hydrogen Paschen broad emission line and other chemical species (Table 1). Therefore, rather than isolating the coronal lines by ‘clipping’ the profiles to the local continuum on the red and blue sides of the line, we carefully modelled all the line complexes around the coronal lines in order to deblend them from neighbouring features (Fig. 2). The resultant coronal line fluxes, their blends, and other observed emission lines are listed in Table 2. In the following, we give details of the analysis.

#### 3.1.1 The continuum

First, the underlying pseudo-continuum is modelled and subtracted in four spectral regions:  $0.7\text{--}1.22$ ,  $1.12\text{--}1.33$ ,  $1.39\text{--}1.53$ , and  $1.65\text{--}2.4 \mu\text{m}$ . The  $1.12\text{--}1.33$  and  $1.39\text{--}1.53 \mu\text{m}$  regions could be satisfactorily fit with a simple power law, whereas the  $0.7\text{--}1.22$  and

$1.65\text{--}2.4 \mu\text{m}$  regions required polynomial models to reproduce the curvature of the pseudo-continuum.

There are no other emission lines in the vicinity of [Si X], therefore its profile could be obtained by simply subtracting the local pseudo-continuum flux. Whilst [Si X] is free from other emission lines, this spectral region is affected by telluric absorption, particularly on the blue side of the line. We were therefore careful to avoid the inclusion of residual telluric features when modelling the pseudo-continuum (see Fig. 2). The coronal lines [S VIII], [S IX], and [Si VI] are all blended with other emission lines. We determined their profiles by modelling the emission line complexes as further described below.

#### 3.1.2 The [S IX] line

The [S IX] coronal line is located on the blue wing of broad Pa  $\beta$ . Schönell et al. (2017) analysed a high-spectral resolution near-IR spectrum of NGC 5548 obtained in 2012 with the Near-Infrared Integral Field Spectrometer (NIFS) at Gemini North. They reported that Pa  $\beta$  has two kinematically distinct components producing a double-peaked broad emission line. Therefore, we decomposed the Pa  $\beta$  emission line using two Gaussians, one red and one blue of the line centre.

The widths of all Gaussians modelling the narrow lines were tied together. In addition to the narrow, forbidden [Fe II] lines at  $1.2570$  and  $1.2791 \mu\text{m}$ , we find two unidentified lines at  $\approx 1.2483$  and  $\approx 1.2612 \mu\text{m}$ . The former unidentified line appears to be present in the spectrum of Schönell et al. (2017), but was not mentioned by the authors, whereas the latter unidentified line is not seen in their spectrum. No transitions near these two wavelengths are reported in observations of classical novae (Wagner & Depoy 1996). We fit these unknown features with narrow Gaussians, but the  $1.2612 \mu\text{m}$  line is very weak and we could only obtain an upper limit on its flux. Therefore, we have not considered this line further in the fits of the individual spectra. In order to not make any prior assumptions about the [S IX] line profile, the narrow window containing the [S IX] line was masked and not used in the fitting process. Having fit for Pa  $\beta$ , [Fe II]  $1.2570 \mu\text{m}$  and the unidentified line at  $1.2483 \mu\text{m}$ , we take the residual flux in the emission line complex as the [S IX] profile (Fig. 2).

#### 3.1.3 The [Si VI] line

The [Si VI] coronal line is blended with both the red wing of the weak hydrogen Br  $\delta$  broad line and the extreme red wing of the hydrogen Pa  $\alpha$  broad line. A very weak H<sub>2</sub> line is also expected at  $1.9570 \mu\text{m}$ , although we did not convincingly detect it. A narrow window containing the [Si VI] line was masked, and all other emission lines were modelled with Gaussians.

We assumed that the broad components of the hydrogen lines Pa  $\alpha$  and Br  $\delta$  have the same double-Gaussian profile as the Pa  $\beta$  broad component (see Section 3.1.2). The amplitude of the broad Br  $\delta$  profile was fixed so as not to exceed the observed flux. Since the width of the narrow Br  $\delta$  line hit the maximum allowed value, we fixed it to that of the narrow Pa  $\beta$  line and fitted only for the flux and velocity offset. The resulting ratio between the Br  $\delta$  and Pa  $\beta$  narrow line fluxes is  $0.14 \pm 0.03$ , which is similar to the value of  $0.11$  expected for Case B and a gas temperature of  $15000 \text{ K}$  (Osterbrock & Ferland 2006). We note that an additional, weak broad Gaussian component was required by the fits in order to adequately model the red wing of Pa  $\alpha$ , but we do not ascribe a particular physical meaning to this component. The residuals of our best-fitting model reveal the profile

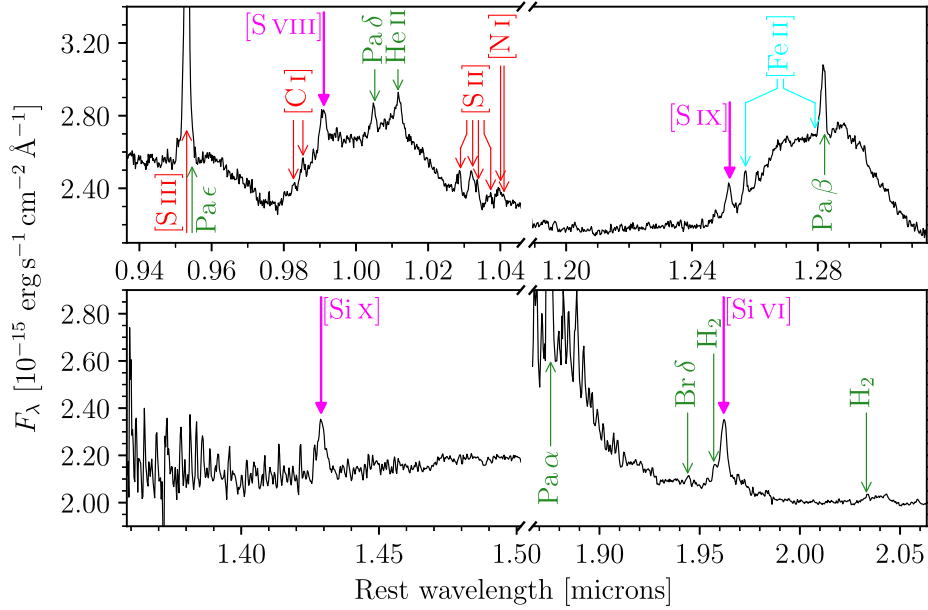


**Figure 1.** Spectral regions in the mean spectrum around the four near-IR coronal lines studied. The coronal lines are labelled in magenta, whereas contaminating permitted and forbidden transitions are labelled in green and red, respectively. Forbidden transitions of iron are labelled in cyan. The wavelengths and fluxes of all the marked emission lines are listed in Table 2.

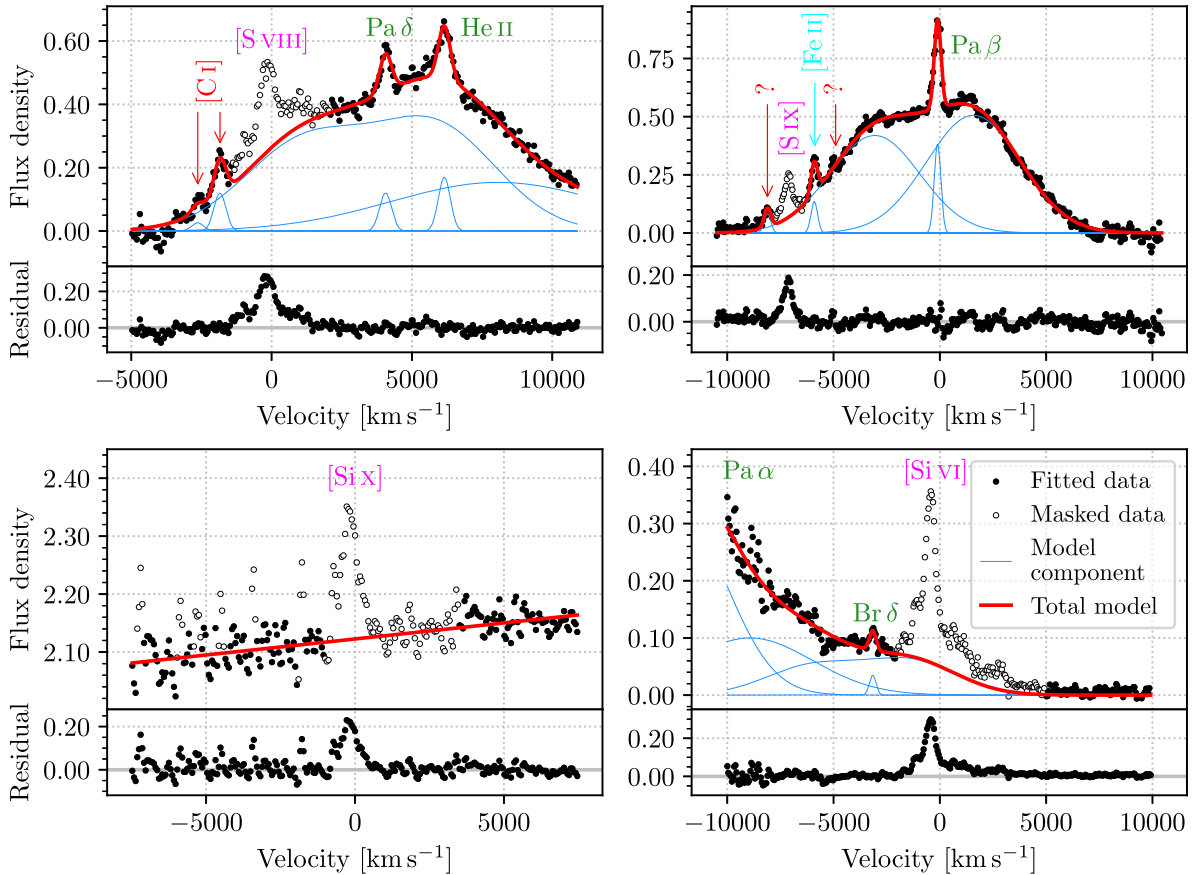


**Figure 2.** The decomposition of emission line blends around the four near-IR coronal lines using the mean spectrum. All coronal lines were masked out and not used in the fitting process. Individual emission lines are shown as blue dotted lines, and the total models are shown as the red solid lines. The bottom panels for each coronal line show the flux residuals across the full emission line complex. All velocities are relative to the expected rest-frame wavelength of the coronal line, except in the case of [S IX], where velocities are relative to Pa  $\beta$ . See Section 3.1 in the text for more details.

**Table 2.** Emission line parameters measured in the mean spectrum.

Ion	$\lambda$ [ $\mu\text{m}$ ]	Line component	Velocity offset	FWHM [ $\text{km s}^{-1}$ ]	Flux [ $10^{-15} \text{ erg s}^{-1} \text{ cm}^{-2}$ ]
(1)	(2)	(3)	(4)	(5)	(6)
[S III]	0.90711			$378 \pm 11$	$13.3 \pm 0.5$
[S III]	0.95332			$365 \pm 7$	$33 \pm 3$
[C I]	0.98268		$+48 \pm 24$	$483 \pm 27$	$0.5 \pm 0.2$
[C I]	0.98530		$+48 \pm 24$	$483 \pm 27$	$2.1 \pm 0.2$
[S VIII]	0.99138	Core	$-119 \pm 15^*$	$737 \pm 39$	$7.3 \pm 0.4$
''		Blue wing			$1.7 \pm 0.4$
''		Red wing			$2.8 \pm 0.7$
H I (Pa $\delta$ )	1.00521	Narrow	$-69 \pm 25$	$461 \pm 26$	$2.9 \pm 0.2$
H I (Pa $\delta$ )		Broad 1	$-2961$	$5091$	
H I (Pa $\delta$ )		Broad 2	$+1680$	$5149$	$109 \pm 11$
He II	1.01264	Narrow	$-7 \pm 18$	$461 \pm 26$	$2.9 \pm 0.2$
He II		Broad	$+1576 \pm 1025$	$8847 \pm 956$	$49 \pm 11$
Unknown	1.2475			$334 \pm 13$	$1.3 \pm 0.2$
[S IX]	1.2523		$-120 \pm 14^*$	$554 \pm 24$	$4.3 \pm 0.2$
[Fe II]	1.25702		$+25 \pm 18$	$334 \pm 13$	$2.2 \pm 0.2$
Unknown	1.2612			$380 \pm 15$	$<0.45$
H I (Pa $\beta$ )	1.28216	Narrow	$-55 \pm 12^*$	$334 \pm 13$	$6.4 \pm 0.3$
H I (Pa $\beta$ )		Broad 1	$-2961 \pm 125$	$5091 \pm 197$	
H I (Pa $\beta$ )		Broad 2	$+1680 \pm 112$	$5149 \pm 141$	$215 \pm 7$
[Si X]	1.430		$-138 \pm 14^*$	$734 \pm 43$	$7.9 \pm 0.6$
H I (Br $\delta$ )	1.94509	Narrow	$-69 \pm 41$	$334$	$0.9 \pm 0.2$
H I (Br $\delta$ )		Broad 1	$-2961$	$5091$	
H I (Br $\delta$ )		Broad 2	$+1680$	$5149$	$39$
[Si VI]	1.9650	Core	$-384 \pm 14^*$	$607 \pm 25$	$13.0 \pm 0.6$
''		Blue wing			$3.6 \pm 0.4$
''		Red wing			$8.7 \pm 0.6$
H <sub>2</sub>	2.0332		$-66 \pm 17^*$	$174 \pm 25$	$0.8 \pm 0.1$
H I (Br $\gamma$ )	2.16612	Narrow	$0 \pm 22$	$389 \pm 46$	$1.3 \pm 0.2$
H I (Br $\gamma$ )		Broad 1	$-2961$	$5091$	
H I (Br $\gamma$ )		Broad 2	$+1680$	$5149$	$43.3 \pm 0.3$

*Note.* The columns are: (1) Ion; (2) vacuum wavelength; (3) fitted emission line component; (4) velocity offset of the emission line peak relative to [S III] 0.95332  $\mu\text{m}$ : narrow line shifts with a significance  $>3\sigma$  are marked \*; (5) full width at half maximum of the emission line component corrected for an instrumental broadening of  $150 \text{ km s}^{-1}$ ; and (6) integrated line flux. We give  $1\sigma$  errors. We note that all H I emission lines are assumed to have the same double-peaked broad-line profile as Pa  $\beta$  and that we list for them only the total broad line flux.

of the relatively strong [Si VI] line. It shows a prominent and extended red wing and excess blue flux in addition to a narrow core (Figs 2 and 3). The width, flux and velocity offset of the core component have been determined by fitting a Gaussian to a region spanning  $\approx 800 \text{ km s}^{-1}$  across the peak of the line (the solid red line in Fig. 3); these are the values reported for the ‘core’ component in Table 2. To determine the fluxes in the wings, we have integrated the excess flux from the peak of the core out to  $\approx -2000 \text{ km s}^{-1}$  on the blue side of the core and  $\approx +3000 \text{ km s}^{-1}$  on the red side. The integration limits for the wings were determined by a visual inspection of the spectrum to determine the maximum velocity extents of the excess flux. Since the red wing in particular is shallow at its extremity, it is likely that an appreciable amount of the integrated flux is just noise. To account for this, we estimate the noise contribution to the integrated flux. We first calculate the noise in the pseudo-continuum in two windows adjacent to the wings. Using this value, we then simulate 1000 Gaussian noise ‘spectra’ on the same velocity grid over which the wings are integrated. The positive fluxes in these mock spectra are integrated, and the mean value gives us an estimate of the amount of noise included in the wings’ flux, which we take to be the uncertainty. These values are reported for the ‘blue wing’ and ‘red wing’ components in Table 2.

### 3.1.4 The [S VIII] line

The [S VIII] coronal line is located near the emission maximum of a blend between the hydrogen Pa  $\delta$  and He II broad emission lines and close to their respective narrow components. This complex also contains the narrow, forbidden lines [C I] 0.9827 and 0.9853  $\mu\text{m}$  and [S II] 1.0290, 1.0323, 1.0339, and 1.0373  $\mu\text{m}$ . We fitted the wavelength region of 0.975–1.027  $\mu\text{m}$ , which excludes the [S II] lines. We again used the broad Pa  $\beta$  profile as a template for the broad hydrogen lines (here Pa  $\delta$ ) and we fitted for its flux only. On the red side of the emission line blend, a single broad Gaussian was adequate to fit the remaining flux from broad He II. Single Gaussians were included to model the [C I], Pa  $\delta$ , and He II narrow lines. The velocity offsets of the two [C I] lines were tied together.

Having modelled and subtracted emission lines other than [S VIII] in the complex, we take the residual flux from our model as the [S VIII] profile (see Fig. 2). The [S VIII] coronal line has a similar profile to that of [Si VI] comprising of a red wing, excess blue flux, and a narrow core (Figs 2 and 3). Measurements of the line core and the blue and red wings have been made in the same manner as for [Si VI], described in Section 3.1.3; the results are reported in Table 2.

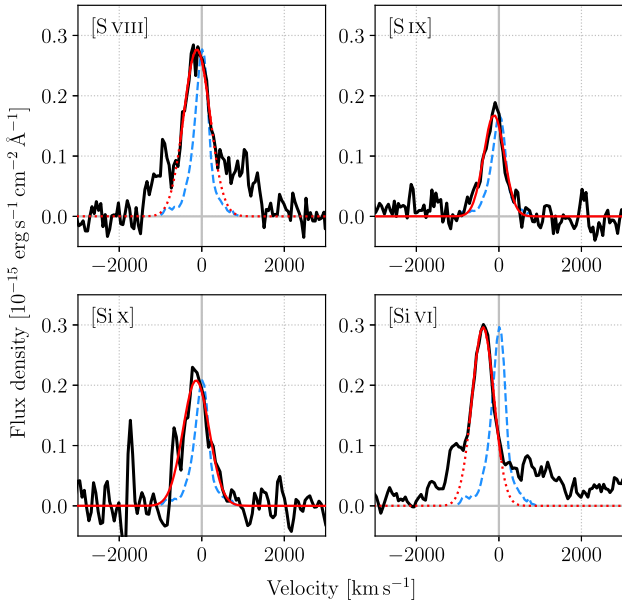


**Figure 3.** The coronal line profiles as extracted from the mean spectrum (black) and fit with Gaussians (red). The total profiles of the [S IX] and [Si X] lines are fit with a single Gaussian, whereas only the central cores of the [S VIII] and [Si VI] lines are fit (solid red lines). For the latter two lines, we additionally show the best-fitting extrapolated across the whole line profile (dotted red lines); blue and red excess flux is evident on these lines. For comparison, the [Si III]  $\lambda 9531$  profile (normalized in amplitude to each coronal line profile) is plotted with a blue dashed line. The four coronal lines are broader than [Si III] and blueshifted with respect to it.

### 3.1.5 Other emission lines

For our study, we have modelled also the hydrogen Br  $\gamma$  broad emission line, since it is of interest for black hole mass determinations in AGN (see Section 4.3), and the [S III]  $\lambda\lambda 9069, 9531$  narrow emission line doublet, since these lines can inform us about the intrinsic profile of transitions from the narrow emission line region.

There are no other broad emission lines in the vicinity of Br  $\gamma$  and we isolated the line from a linear local continuum. The broad component was modelled with the same profile as the other hydrogen lines and we fit only for its flux. In addition to a narrow Gaussian for Br  $\gamma$ , a second narrow Gaussian was added to model the H<sub>2</sub> 2.0332  $\mu\text{m}$  emission line, which sits on the blue wing of broad Br  $\gamma$ .

The [S III]  $\lambda\lambda 9069, 9531$  narrow emission line doublet is a strong feature in our spectra. We subtracted the hydrogen Pa  $\epsilon$  broad emission line from beneath the [S III] lines, again using broad Pa  $\beta$  as a template. We also subtracted a narrow Gaussian line at the rest-frame wavelength of Pa  $\epsilon$  from the [S III]  $\lambda 9531$  line profile. Having accounted for the Pa  $\epsilon$  emission, each [S III] line was adequately fit with a single Gaussian of FWHM  $\approx 370 \text{ km s}^{-1}$ . No significant velocity shift was measured between the two [S III] lines. The centroid velocity shifts of all other lines measured in the mean spectrum were measured relative to [S III]  $\lambda 9531$ . The observed flux ratio of [S III]  $\lambda 9531$ /[S III]  $\lambda 9069 = 2.5 \pm 0.1$  is consistent with the theoretical value of 2.58.

### 3.2 The single-epoch spectra

Because of the lower quality of the single-epoch spectra relative to the mean spectrum, multi-Gaussian fits to the emission line complexes were not always successful in reliably isolating the coronal lines.

Therefore, we used their emission-line profiles determined in the mean spectrum as a guide. Having subtracted the underlying broad-band continuum following the method described in Section 3.1.1, we then performed a fit to the emission line blend. The mean Pa  $\beta$  profile was again used as a template for all of the hydrogen lines; the template was rescaled in flux to match the hydrogen lines in the single-epoch spectra. Each narrow line profile was modelled as a single Gaussian with its parameters taken from the fit to the same line in the mean spectrum. If necessary, small scaling adjustments were made to the narrow lines to improve the fit. To some spectra, we added a local continuum to correct cases in which we judged the broad-band continuum placement could be improved. The local continuum and contaminating lines were adjusted to obtain a good fit to the data, then subtracted from the spectrum, leaving just the coronal line profile. As can be seen in Figs 5–10, the residuals away from the coronal line are generally featureless (with the exception of imperfect telluric correction around [Si X]), indicating that this procedure generally worked well. However, the coronal line profiles in a few epochs were of very poor quality, and we have excluded them for our further studies. As for the mean spectrum, the fluxes, widths, and velocity offsets of the narrow line cores are determined by fitting a Gaussian to the isolated emission line profile. Again, for [S VIII] and [Si VI] we fit only the central portion of the profiles (within a few hundred  $\text{km s}^{-1}$  of the peak) to avoid the wings on either side of the line.

Because the coronal lines are low-contrast features in our spectra the FWHM and flux measurements are very sensitive to the placement of the underlying pseudo-continuum. If the continuum is placed too high, for example, then both the FWHM and flux will be underestimated in the fitted profile. This is an issue in the single-epoch spectra, in which the precise continuum placement is less certain than in the high-S/N mean spectrum. We therefore calculate the range in both FWHM and flux that results from moving the local continuum to its highest and lowest plausible levels (i.e.  $\pm 1\sigma$ ). The value of  $\sigma$ , the noise in the continuum, is calculated from the standard deviation of flux points about the mean value in featureless windows near to each coronal line (and typically this noise was  $\sim 1$  per cent of the continuum flux). This additional uncertainty was added in quadrature to the Gaussian measurement uncertainties calculated by the fitting algorithm. A similar approach was taken to estimate the uncertainties on the [S VIII] and [Si VI] wings; we calculate the error range from the maximum and minimum excess flux integrated with the continuum is moved  $\pm 1\sigma$ . Because the blue wing is weak and the red wing is very shallow at its extremity, this results in rather large uncertainties for the wings (particularly in the noisy part of the spectrum containing [S VIII]) and there are several epochs where no flux in excess of the Gaussian core is detected with confidence.

Our results for the four near-IR coronal lines as well as the strong [S III]  $\lambda 9531$  line are shown in Figs 5–10. The fluxes of the line cores and wings over the course of the campaign are recorded in Table 3.

### 3.3 Optical iron coronal lines

During one of our other observing programmes, we obtained a high-resolution optical spectrum of NGC 5548 in 2015 March at the William Herschel Telescope (WHT), a 4-m telescope on La Palma. We dereddened this spectrum using  $E(B - V) = 0.0168$  (Schlafly & Finkbeiner 2011) and the extinction curve of Cardelli, Clayton & Mathis (1989). The spectrum contains six high-ionization forbidden lines of iron: [Fe VII]  $\lambda 3759, 5159, 5721, 6087$ , [Fe X]  $\lambda 6374$ , and [Fe XI]  $\lambda 7892$ . With the exception of [Fe X] these lines are unblended

**Table 3.** Fluxes of the cores and blue and red wings in the profiles of [S III]  $\lambda 9531$  and the near-infrared the coronal lines.

Date	[S III] Core	[S VIII]			[S IX] Core	[Si X] Core	[Si VI]		
		Blue wing	Core	Red wing			Blue wing	Core	Red wing
Mean spectrum	33 $\pm$ 3	1.7 $\pm$ 0.4	7.3 $\pm$ 0.4	2.8 $\pm$ 0.7	4.3 $\pm$ 0.2	7.9 $\pm$ 0.6	3.6 $\pm$ 0.4	13.0 $\pm$ 0.6	8.7 $\pm$ 0.6
602 16/08/02	34 $\pm$ 2	3.5 $\pm$ 1.8	8.9 $\pm$ 3.4	4.4 $\pm$ 3.2	4.5 $\pm$ 1.3	7.7 $\pm$ 2.5	2.0 $\pm$ 1.1	13.2 $\pm$ 1.7	18.7 $\pm$ 2.4
611 16/08/11	35 $\pm$ 2	1.5 $\pm$ 1.9	7.2 $\pm$ 5.0	4.7 $\pm$ 2.9	–	5.7 $\pm$ 2.6	1.7 $\pm$ 1.3	12.4 $\pm$ 1.8	16.7 $\pm$ 2.7
743 16/12/21	–	–	–	–	3.6 $\pm$ 1.3	6.0 $\pm$ 2.5	–	–	–
759 17/01/06	34 $\pm$ 2	<4.6	8.0 $\pm$ 3.7	7.0 $\pm$ 4.1	3.6 $\pm$ 1.8	7.9 $\pm$ 2.7	2.4 $\pm$ 0.5	13.3 $\pm$ 1.7	<2.1
773 17/01/20	34 $\pm$ 2	4.1 $\pm$ 1.8	5.3 $\pm$ 3.4	<6.2	5.2 $\pm$ 1.4	7.2 $\pm$ 2.7	3.9 $\pm$ 0.7	11.3 $\pm$ 1.7	3.4 $\pm$ 1.8
777 17/01/24	33 $\pm$ 2	–	–	–	–	6.5 $\pm$ 3.6	4.7 $\pm$ 1.1	14.7 $\pm$ 2.3	5.5 $\pm$ 2.4
789 17/02/05	33 $\pm$ 1	3.4 $\pm$ 2.2	6.6 $\pm$ 3.3	<7.2	6.1 $\pm$ 1.7	8.1 $\pm$ 2.6	4.3 $\pm$ 0.8	13.9 $\pm$ 1.7	3.4 $\pm$ 1.8
799 17/02/15	35 $\pm$ 2	<3.8	4.9 $\pm$ 3.3	3.6 $\pm$ 3.5	2.5 $\pm$ 1.3	6.6 $\pm$ 2.6	4.3 $\pm$ 0.9	14.7 $\pm$ 1.9	4.9 $\pm$ 2.0
804 17/02/24	34 $\pm$ 1	2.4 $\pm$ 1.7	4.5 $\pm$ 3.3	3.4 $\pm$ 3.4	4.1 $\pm$ 1.5	5.5 $\pm$ 2.6	2.8 $\pm$ 1.1	11.5 $\pm$ 1.8	3.8 $\pm$ 2.4
829 17/03/17	35 $\pm$ 2	2.9 $\pm$ 1.9	5.3 $\pm$ 3.2	3.7 $\pm$ 3.3	4.2 $\pm$ 1.7	5.8 $\pm$ 2.6	2.3 $\pm$ 0.7	11.3 $\pm$ 1.9	2.2 $\pm$ 1.7
834 17/03/22	35 $\pm$ 2	<2.7	6.3 $\pm$ 3.3	5.3 $\pm$ 2.4	5.5 $\pm$ 1.5	8.2 $\pm$ 3.0	2.3 $\pm$ 1.1	15.3 $\pm$ 2.0	<5.1
882 17/05/09	33 $\pm$ 2	–	–	–	3.8 $\pm$ 1.8	6.7 $\pm$ 2.6	3.1 $\pm$ 0.7	12.0 $\pm$ 1.7	4.1 $\pm$ 1.5
898 17/05/25	33 $\pm$ 3	4.0 $\pm$ 2.7	8.9 $\pm$ 4.7	7.0 $\pm$ 4.5	5.2 $\pm$ 1.7	9.1 $\pm$ 3.1	4.0 $\pm$ 1.1	15.3 $\pm$ 1.7	4.9 $\pm$ 2.4
914 17/06/10	34 $\pm$ 2	–	–	–	–	–	3.7 $\pm$ 0.8	13.2 $\pm$ 1.8	6.7 $\pm$ 1.7
924 17/06/20	33 $\pm$ 2	<6.4	12.5 $\pm$ 6.9	6.3 $\pm$ 5.0	3.2 $\pm$ 1.9	7.3 $\pm$ 4.5	4.8 $\pm$ 1.3	10.5 $\pm$ 1.7	9.9 $\pm$ 2.9
932 17/06/28	33 $\pm$ 2	3.0 $\pm$ 1.5	7.8 $\pm$ 3.3	7.7 $\pm$ 2.8	1.6 $\pm$ 1.2	7.0 $\pm$ 3.4	5.6 $\pm$ 1.1	9.7 $\pm$ 1.8	9.3 $\pm$ 2.5
937 17/07/03	33 $\pm$ 2	2.7 $\pm$ 1.6	9.4 $\pm$ 3.4	5.3 $\pm$ 2.9	–	–	–	–	–
rms	0.84 (2.5 %)	0.62 (20 %)	2.25 (32 %)	1.50 (29 %)	1.25 (31 %)	1.03 (15 %)	1.18 (35 %)	1.69 (13 %)	5.22 (79 %)

Note. The observation date is given in the formats MJD – 57000 and YY/MM/DD and the fluxes are in units  $10^{-15}$  erg s $^{-1}$  cm $^{-2}$ .

so we simply measure their profiles with a single Gaussian plus linear local continuum. [Fe X] is blended with [O I]  $\lambda 6363$  so we first determine the profile of [O I]  $\lambda 6300$  and use this as a template for [O I]  $\lambda 6363$ , assuming a 1:3 flux ratio. We assume [O III]  $\lambda 5007$  to be at rest within NGC 5548 and measure all other line velocity shifts relative to it. The FWHMs of the lines are all corrected for instrumental broadening, assuming this is  $\sim 250$  km s $^{-1}$  for the ISIS instrument on the WHT. The properties of these lines are reported in Table 4.

## 4 RESULTS

### 4.1 The mean coronal line profiles

Fig. 3 shows the profiles of the four near-IR coronal lines as observed in the mean spectrum. In all four cases, the central (core) part can be modelled well with a single Gaussian. It is intriguing to notice that both the [S VIII] and [Si VI] coronal lines show significant excess flux blue- and red-ward of the core, whereas the [S IX] and [Si X] coronal lines do not.

In Fig. 4 we show the coronal line and [S III] widths and velocity shifts as a function of both their ionization potentials and critical densities. The coronal line (core) profiles are all broader than the [S III] doublet lines, with line widths of FWHM  $\sim 500$ – $800$  km s $^{-1}$ , compared with  $\approx 370$  km s $^{-1}$  for [S III]. Whilst we have only five data points, Fig. 4 shows a trend of increasing FWHM with ionization potential up to  $\approx 300$  eV. It is clear in Fig. 4 that all four coronal lines have emission line peaks blue-shifted with respect to [S III]. The [S VIII], [S IX], and [Si X] lines have very similar average velocity offsets of  $\approx -130$  km s $^{-1}$ ; curiously, the lowest-ionization potential coronal line [Si VI] has a much greater velocity offset of  $\approx -380$  km s $^{-1}$ , so there is no simple relationship between the velocity shift and ionization potential. We also measured the velocity shifts of the other forbidden, narrow emission lines in the mean spectrum, with none of them having a significant velocity shift (see

Table 2). Although it is clear that the coronal lines have higher critical densities and both greater line widths and velocity shifts than [S III], no simple trend with critical density is observed between the four coronal lines.

### 4.2 The coronal line variability

The low-ionization narrow forbidden emission lines are assumed to be produced in AGN at distances from the central engine large enough to not show significant flux variability over the course of decades. But the optical narrow-line reverberation results for NGC 5548 show that the [O III]  $\lambda 5007$  line emitting region is more nuclear than expected, with an extent of only 1–3 pc and a density of  $\sim 10^5$  cm $^{-3}$  (Peterson et al. 2013). Since our campaign extends over the course of roughly a year, we can still assume that the flux of the [S III]  $\lambda 9531$  line is not variable. This expectation is confirmed by the results in Table 3 and Fig. 5: the rms variability of [S III]  $\lambda 9531$  is  $\approx 8.4 \times 10^{-16}$  erg s $^{-1}$  cm $^{-2}$ , only around 2.5 per cent of the mean line flux. The width of this line is also stable during our campaign, with two-thirds of data points being consistent with the mean value to within  $1\sigma$ .

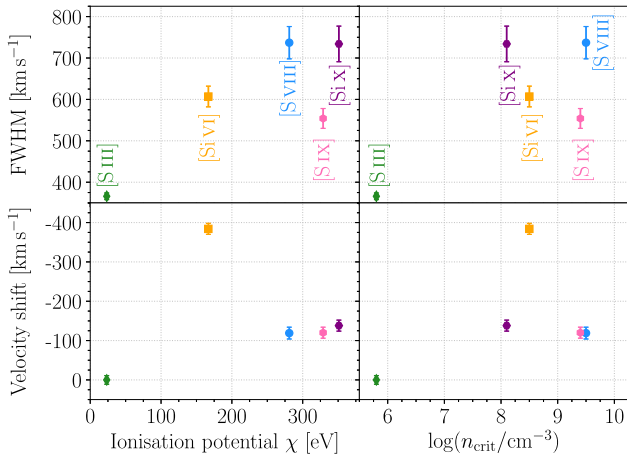
#### 4.2.1 The [Si VI] and [S VIII] lines

The [Si VI] line is the strongest of the four near-IR coronal lines in our spectra; we reliably isolated its profile in 15/18 spectra (Fig. 6). We measure a maximum flux variability of  $\sim 50$  per cent for the [Si VI] line core, with rms  $\approx 13$  per cent (Table 3). In addition, we observe variable excess emission blue- and red-ward of the line core. Both of these flux excesses are relatively broad, with the blue- and red-shifted part stretching over  $\sim 2000$  and  $\sim 3000$  km s $^{-1}$ , respectively (Fig. 8), and in the mean spectrum their combined flux is similar to the flux in the core of the line. The red flux excess variability shows cyclical behaviour: it is most prominent in the first spectra with a flux exceeding that in the line core, becomes weak by the middle of

**Table 4.** Properties of optical iron coronal lines and measurements from the 2015 WHT spectrum.

Ion	$\lambda$ [Å]	$\chi$ [eV]	$\log(n_{\text{crit}})$ [cm <sup>-3</sup> ]	Velocity offset [km s <sup>-1</sup> ]	FWHM [km s <sup>-1</sup> ]	Flux [10 <sup>-15</sup> erg s <sup>-1</sup> cm <sup>-2</sup> ]
(1)	(2)	(3)	(4)	(5)	(6)	(7)
[Fe VII]	3759	99.1	7.60	-207 ± 17	559 ± 38	16.9 ± 1.5
''	5159	99.1	6.54	-126 ± 21	<250	3.01 ± 0.80
''	5721	99.1	7.57	-111 ± 11	485 ± 18	10.5 ± 0.5
''	6087	99.1	7.64	-201 ± 9	632 ± 13	20.1 ± 0.5
[Fe X]	6374	233.6	8.64	-188 ± 15	605 ± 46	5.24 ± 0.51
[Fe XI]	7892	262.1	8.81	-212 ± 24	579 ± 57	4.44 ± 0.56

*Note.* The columns are: (1) Ion; (2) vacuum wavelength; (3) ionization potential; (4) critical density for  $\log(T/K) = 4$ ; (5) velocity offset of the emission line peak relative to [O III]  $\lambda 5007$ ; (6) full width at half maximum of the emission line component corrected for an instrumental broadening of 250 km s<sup>-1</sup>; and (7) line flux. We give 1 $\sigma$  errors.

**Figure 4.** FWHM (top) and centroid velocity shift (bottom) of the coronal line and [S III]  $\lambda 9531$  cores, measured in the mean spectrum, as a function of ionization potential (left) and critical density (right).

the campaign, and increases in flux again at later epochs (Fig. 6 and Table 3). In the second part of the campaign (after the seasonal gap), the blue excess varies in the same manner as the red excess; however, the blue excess is weakest in the first observing epochs, unlike the red excess, which is strongest.

The [S VIII] coronal line was strong enough to be reliably isolated in 13/18 single-epoch spectra (Fig. 7). The [S VIII] line core is much more variable than that of the [Si VI] line, with maximum flux changes by a factor of  $\approx 3$  (Table 3). Like for the [Si VI] line, we observe variable and broad excess emission blue- and red-ward of the line core (Fig. 8), but in the mean spectrum, their combined flux is only about half that of the core of the line. Given that the [S VIII] line is also on average a factor of  $\sim 2$  weaker than the [Si VI] line, the isolation of the excess fluxes in the single-epoch spectra is more problematic. However, there is a trend for this excess emission to be strongly variable (by factors of a few) also in the [S VIII] coronal line.

In Fig. 8, we overplot all of the single-epoch line profiles of both [S VIII] and [Si VI] for easier comparison. In [Si VI], it is clear that most of the variability in the profile is in the broad wings, with the narrow core showing relatively little variation from the mean. This is reflected in the rms variability measured for the different line components (Table 3). Because of the noisier data, it is more difficult to see the same behaviour in the [S VIII] line and the rms variability of the core and blue and red wings are similar ( $\approx 30$  per cent). In Fig. 8, we highlight two spectra with strong and weak wings but similar

cores, so visually at least a similar trend as observed in [Si VI] can be discerned.

#### 4.2.2 The [Si X] and [Si IX] lines

The [Si X] line is the second strongest coronal line in our spectra and is free of blends. However, it is located in a region of telluric absorption, which is strongest blueward of it. We extracted its profile in 15/18 single-epoch spectra (Fig. 9). Its rms flux variability (15 per cent) is very similar to that of the [Si VI] core.

[Si X] is the weakest near-IR coronal line in our study but was strong enough to be reliably isolated in 13/18 single-epoch spectra. It shows a similar variability range to the [S VIII] line core, with maximum flux changes by a factor of  $\sim 3$  and rms of 31 per cent, but without a clear trend (Fig. 10).

#### 4.2.3 Trends in coronal line variability

As can be seen from Table 3, the coronal line cores show a slightly higher degree of variability than that of [S III]  $\lambda 9531$ : rms  $\approx 10$ –30 per cent for the coronal lines compared with rms = 2.5 per cent for [S III]. Figs 6, 7, 9, and 10 suggest that there is a correspondence between the measured FWHM and flux of the coronal line cores, in the sense that as the flux increases, the line becomes broader. However, this variability is not statistically significant and simple fits for a constant line flux return  $\chi^2_{\nu} = 0.27, 0.77, 0.14,$  and  $0.85$  for the [S VIII], [Si IX], [Si X], and [Si VI] line cores, respectively. Given the substantial uncertainties, we cannot make strong statements about the variability of the narrow line cores.

It is clear from Figs 6–8 that most of the variability in the coronal line profiles is in the wings of [S VIII] and [Si VI]. Flux variations in the [Si VI] red wing are statistically significant and we can reject the null hypothesis that the variability is purely statistical with greater than 99.99 per cent confidence. A fit of constant flux to the [Si VI] blue wing light curve is poor ( $\chi^2_{\nu} = 1.45$ ), suggesting variability of the blue wing also, but the variability is less significant than in the red wing ( $p \approx 0.12$ ). In Fig. 11, we show the variability of the [Si VI] and [S VIII] broad red wings and compare them to those of the hot dust. Because of the noisier data, trends in the raw [S VIII] red wing light curve (Fig. 7d) are less clear. We have therefore binned the light curve to better show the long-term trend, and in Fig. 11, we show the error-weighted average and standard deviations from the mean of consecutive flux points, as indicated. The dust light curve is derived from spectroscopic data, with fluxes integrated over a narrow emission line free region near the centre of the  $H$

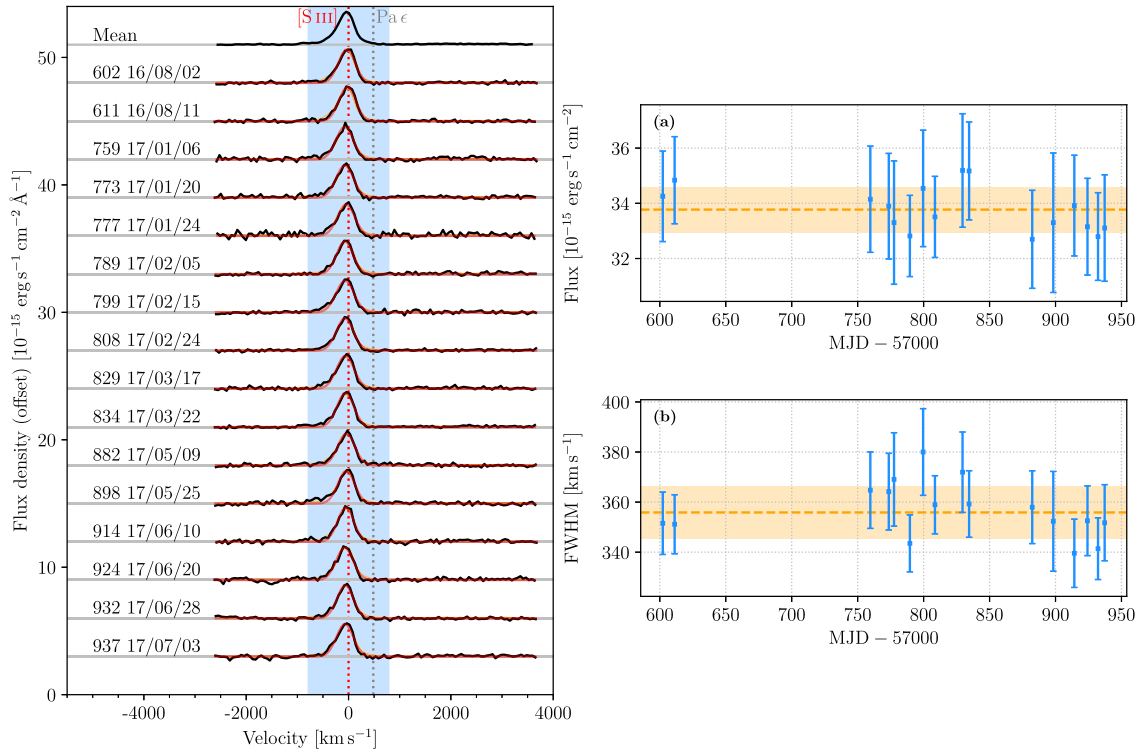


**Figure 5.** The [S III]  $\lambda 9531$  emission line in the mean and single-epoch spectra. Left-hand panel: [S III] emission line profiles isolated from other emission lines and the underlying continuum (black). The location of the subtracted contaminating emission lines is indicated with a grey dashed line. The [S III] profile extracted from the mean spectrum is shown in the individual spectra by the thin orange line. In each spectrum, the blue-shaded region was fitted with a single Gaussian (red line). Each spectrum is labelled with the observation date in the formats MJD – 57000 and YY/MM/DD. Right-hand panels (a) and (b) show variations of the line core flux and FWHM obtained from the Gaussian fit. The error-weighted mean flux and FWHM are shown by the orange dashed lines, and the orange shaded regions are the mean  $\pm\sigma$ . We plot  $1\sigma$  errors.

photometric band (1.55–1.60  $\mu\text{m}$ ; Landt et al. 2019). We observe a strong similarity in the shapes of the dust and the coronal line red wing light curves (particularly [Si VI]): the fluxes are initially high, but weaken substantially during the gap in observations between MJD 57621 and 57743; the fluxes remain low in the middle of the campaign, before a systematic rise from MJD 57882 onwards.

### 4.3 The black hole mass from near-IR emission line ratios

Rodríguez-Ardila et al. (2020) presented a novel method to calculate black hole masses using the flux ratio of coronal lines to low-ionization permitted lines (see also Prieto et al. 2022). From flux measurements made by Riffel, Rodríguez-Ardila & Pastoriza (2006), Rodríguez-Ardila et al. (2020) calculate the flux ratio [Si VI]/Br  $\gamma = (9.97 \pm 0.86)/(16.27 \pm 2.0) = 0.61 \pm 0.09$  from which they determined a black hole mass of  $6.7 \times 10^6 M_{\odot}$ . Considering the total flux (core + wings) in the [Si VI] line, we calculate [Si VI]/Br  $\gamma = (25.3 \pm 0.9)/(43.3 \pm 0.3) = 0.58 \pm 0.02$  from our mean spectrum, which is consistent within the uncertainties with the value determined by Rodríguez-Ardila et al. (2020) and therefore gives the same black hole mass. Therefore, although the absolute fluxes of the lines differ by more than a factor two between the 2002 IRTF spectrum of Riffel et al. (2006) and our 2016–17 mean spectrum, the flux ratio has not changed, as one would expect if the flux ratio reflects the black hole mass.

We note that using the [Si VI] core flux only results in the flux ratio =  $0.31 \pm 0.01$  and so the estimated black hole mass is approximately four times greater at  $2.6 \times 10^7 M_{\odot}$ , much closer to the

$3.2 \times 10^7 M_{\odot}$  obtained by Pancoast et al. (2014) via reverberation mapping. The mass obtained from the total [Si VI] line flux is 0.66 dex discrepant with the Pancoast et al. (2014) estimate, whereas the mass from the core flux is only 0.09 dex discrepant. These compare with a 0.44 dex scatter in black hole mass reported by Rodríguez-Ardila et al. (2020) for their scaling relation.

## 5 PHOTOIONIZATION MODELS

AGN coronal lines are thought to be photoionized by the soft X-ray nuclear continuum. Since ionic species are most effectively produced by photons with energies just above their ionization potentials, the flux ratios of lines with different ionization potentials will depend on the shape of the ionizing SED. The shape of the ionizing SED depends not just on the properties of the accretion flow (the black hole mass, accretion rate, electron temperature and optical depths of the warm and hot coronae, etc.) but also on extrinsic factors such as obscuration of the ionizing source by gas and dust. This is of particular relevance in studies of NGC 5548 in which a persistent obscurer, first reported by Kaastra et al. (2014), strongly absorbs the nuclear soft X-ray emission along certain lines of sight. Kaastra et al. (2014) described the obscurer as a persistent, clumpy, ionized gas outflow on scales of only a few light-days from the nucleus. Dehghanian et al. (2019) interpreted it as the upper, line-of-sight component of an accretion disc wind; the wind originates interior to the BLR and its dense base shields the BLR from the nuclear continuum source. We know that this obscurer was present during the 2016–17 near-IR spectroscopic campaign because of the

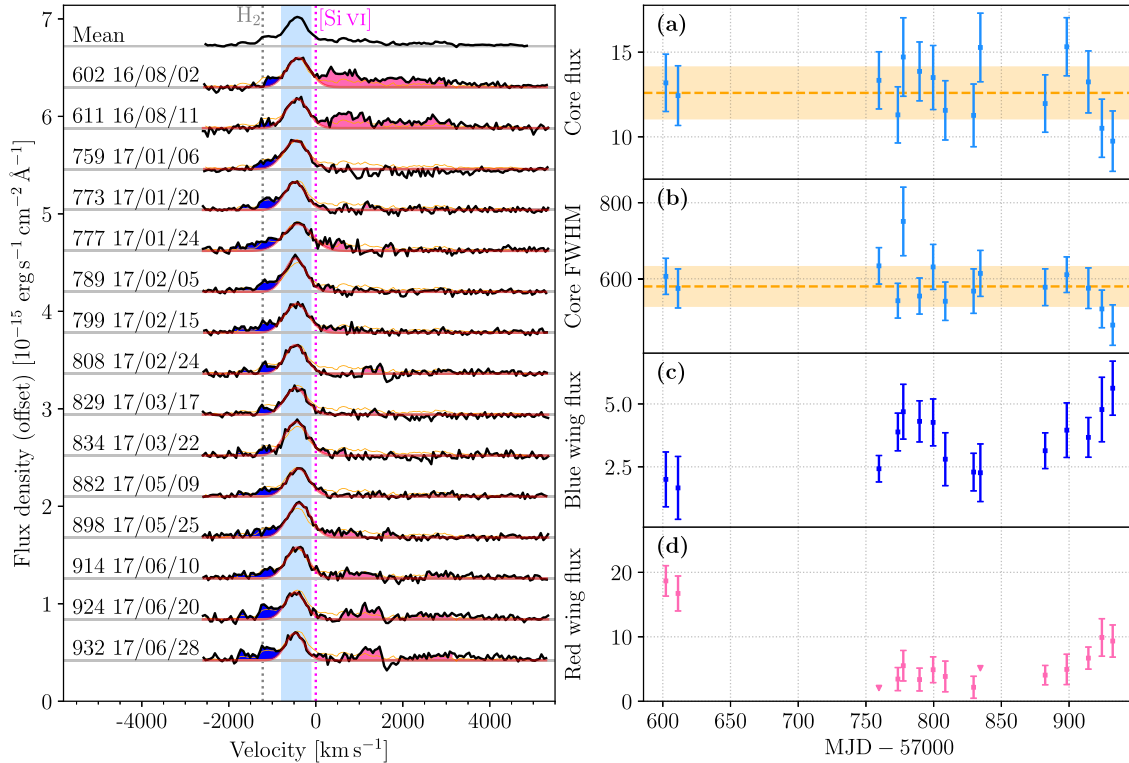


**Figure 6.** The [Si VI] coronal line in the mean and single-epoch spectra. Left-hand panel: [Si VI] emission line profiles isolated from other emission lines and the underlying continuum (black). The locations of the contaminating emission lines are indicated with grey dashed lines; the rest-frame velocity of the coronal line is indicated by the magenta dotted line. The [Si VI] profile extracted from the mean spectrum is shown in the individual spectra by the thin orange line. In each spectrum, the light blue shaded region was fitted with a single Gaussian (red line). Each spectrum is labelled with the observation date in the formats MJD – 57000 and YY/MM/DD. Right-hand panels (a) and (b) show the flux and FWHM (in  $\text{km s}^{-1}$ ) of this Gaussian. The error-weighted mean flux is shown by the orange dashed line, and the orange shaded region spans the mean  $\pm \sigma$ . Panels (c) and (d) show the excess flux above the fitted Gaussian on the blue and red sides of the line centre, respectively. The excess fluxes which were integrated are shaded blue and pink in the left-hand panel. All fluxes are in units  $10^{-15} \text{ erg s}^{-1} \text{ cm}^{-2}$ . We plot  $1\sigma$  errors.

low-flux state NGC 5548 was observed in and the presence of persistent, broad He I  $1.08 \mu\text{m}$  absorption associated with the obscurer (Wildy et al. 2021).

Mehdipour et al. (2015) presented two SEDs based on 2013–14 X-ray observations: one seen through the obscurer, and the intrinsic nuclear SED. We show these SEDs in Fig. 12, where we also mark the ionization potentials of the near-IR coronal lines. Clearly, the coronal line emission would be strongly affected by the obscurer if it intervenes between the coronal line gas and the X-ray source. We do not know *a priori* the location of the coronal line emitting gas, and therefore we can explore whether the line emission predicted by the obscured or unobscured SED better match our observations. Therefore, we used both SEDs in the photoionization code CLOUDY (v17; Ferland et al. 2017) to make predictions about the resultant line emission.

### 5.1 The CLOUDY parameter region

We used the fluxes of the coronal line cores reported in Table 2,<sup>1</sup> and calculated the equivalent widths (EWs) of the lines relative to the  $1215 \text{ \AA}$  continuum flux of the Mehdipour et al. (2015) SEDs. Subsequently, we searched the parameter space for regions which

<sup>1</sup>For [S VIII] and [Si VI] these are the line core fluxes (excluding the wings).

reproduced the observed emission line EWs within uncertainties of  $\approx 30$  per cent. Because we expect that the [S III]-emitting gas is not co-spatial with the coronal line gas, the CLOUDY predictions for [S III] emission can be used to discriminate between models. For example, regions that predict substantial [S III] emission or overpredict the observed flux may be ruled out as potential sites for the coronal line gas. On the other hand, regions that produce little or no [S III] are still viable, since this emission line flux could come from elsewhere. We additionally considered the EWs of the optical Fe coronal lines (Section 3.3) to aid our search. We note that these lines were measured in a spectrum from 2015 March and are therefore non-contemporaneous with our near-infrared data from 2016–17. Flux variability of a factor  $\sim 2$  was seen in the [Fe VII] lines over  $\approx 5$  yr (Landt et al. 2015b). Given this level of intrinsic variability (and some uncertainty in the absolute flux scaling of the optical spectrum), we reasonably expect the optical coronal lines to have fluxes within a factor  $\approx 2$ –3 of those we measured in the 2015 spectrum.

Our CLOUDY models are ‘luminosity cases’ similar to the studies of Ferguson et al. (1997) and Baldwin et al. (1995). This means that we have used the obscured and unobscured SEDs with their corresponding bolometric luminosities estimated by Mehdipour et al. (2015). In particular, for the unobscured case, the bolometric luminosity is  $\log(L_{\text{bol}}/\text{erg s}^{-1}) = 44.2$ , whereas, for the obscured case, it decreases to  $\log(L_{\text{bol}}/\text{erg s}^{-1}) = 43.5$ . Below, we compare all results to the observed values of the coronal lines from the 2016–

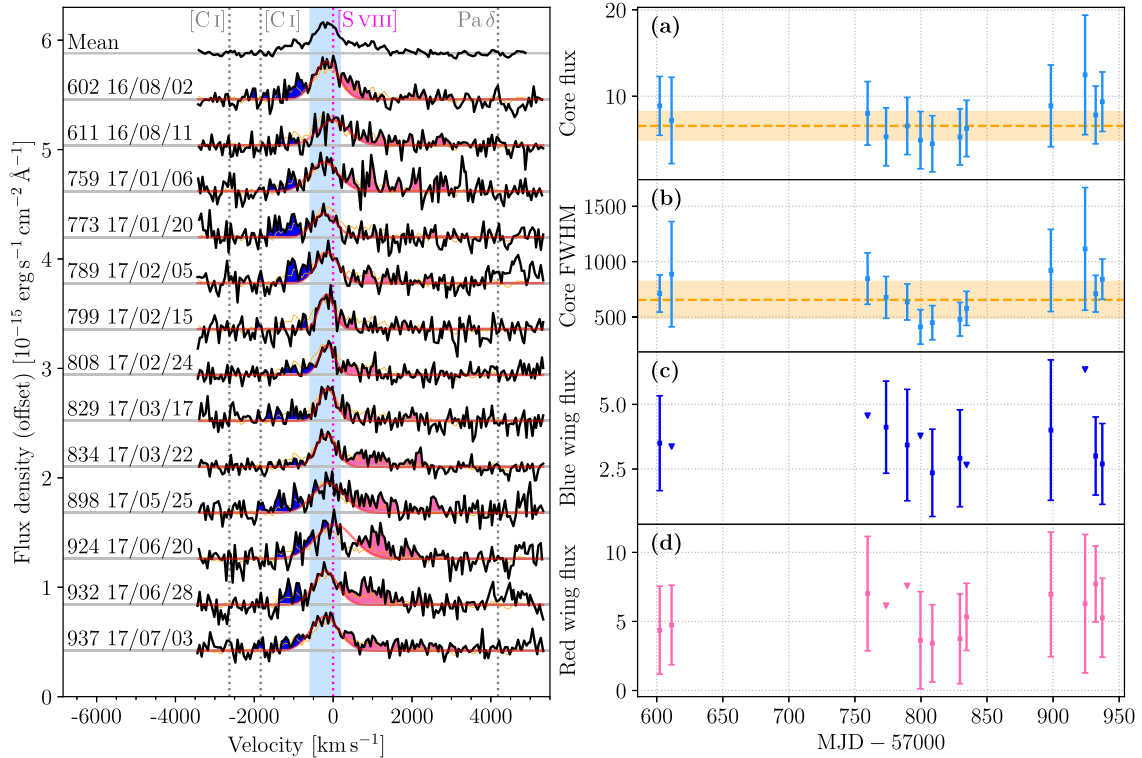


**Figure 7.** The [S VIII] coronal line in the mean and single-epoch spectra. Description as in Fig. 6.

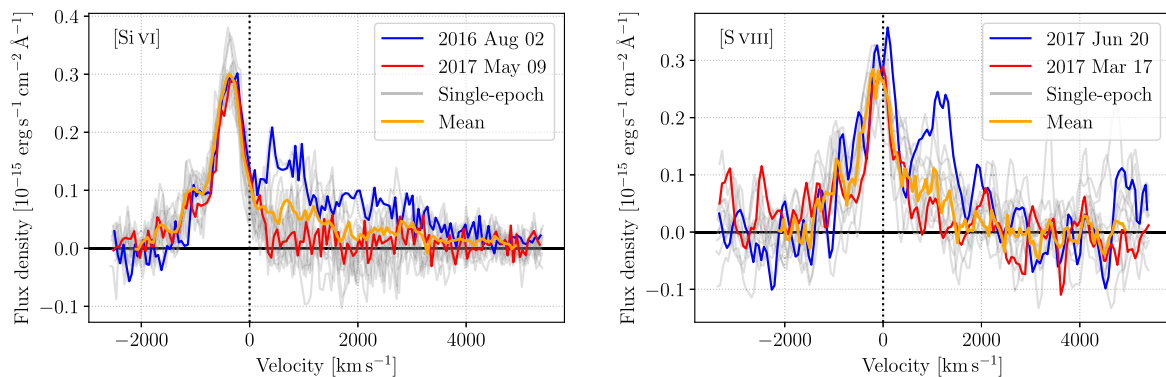


**Figure 8.** The variability of the [Si VI] and [S VIII] coronal line profiles. All extracted profiles are shown in grey and the mean line profiles in orange. An epoch with strong (weak) wings is highlighted in blue (red). The single-epoch [S VIII] profiles have been smoothed slightly for clarity.

17 campaign of Landt et al. (2019). While a three-year time span between the SEDs and the coronal lines probably slightly affects the results, it is also possible that the SEDs were quite different in 2016, which would lead to very different predictions. For this reason, we choose not to fine-tune the CLOUDY results, and we only propose them as a possible solution while we emphasize the importance of the approach. For the future application of the method, it would be beneficial to measure both the emission lines and ionizing continuum in the same time period.

Another source of uncertainty is the column density: the hydrogen column density of the possible coronal line emitting cloud is unknown. The stopping criteria for the CLOUDY models is set to be the column density of the cloud, which is assumed to be  $\log(N_{\text{H}}/\text{cm}^{-2}) = 23$  during most of our calculations. This is a typical value assumed for the coronal line emitting regions; however, it is not measured

and can be a different value, so we have also created some models using  $\log(N_{\text{H}}/\text{cm}^{-2}) = 22$  and 22.5. The cloud has an ionization structure with the highest ionization lines forming near its illuminated face and the lowest ionization lines forming near the shielded face. Decreasing the column density of the cloud will not dramatically affect the higher ionization lines but will reduce the intensity of the low-ionization lines. To check this claim, we created two obscured models with different column densities ( $\log[N_{\text{H}}/\text{cm}^{-2}] = 22$  and 23) and a similar hydrogen density of  $\log(n_{\text{H}}/\text{cm}^{-3}) = 5$ . Both clouds were located at the same distance of  $\log(R/\text{cm}) = 18$ . The CLOUDY calculations indeed show that decreasing the column density by 1 dex (from  $\log[N_{\text{H}}/\text{cm}^{-2}] = 23$  to 22) reduces the EW of high ionization lines only by 15–30 per cent, while the low ionization lines become at least 60 per cent weaker. Therefore, we think that the variation of the column density does not strongly affect the high-ionization lines but

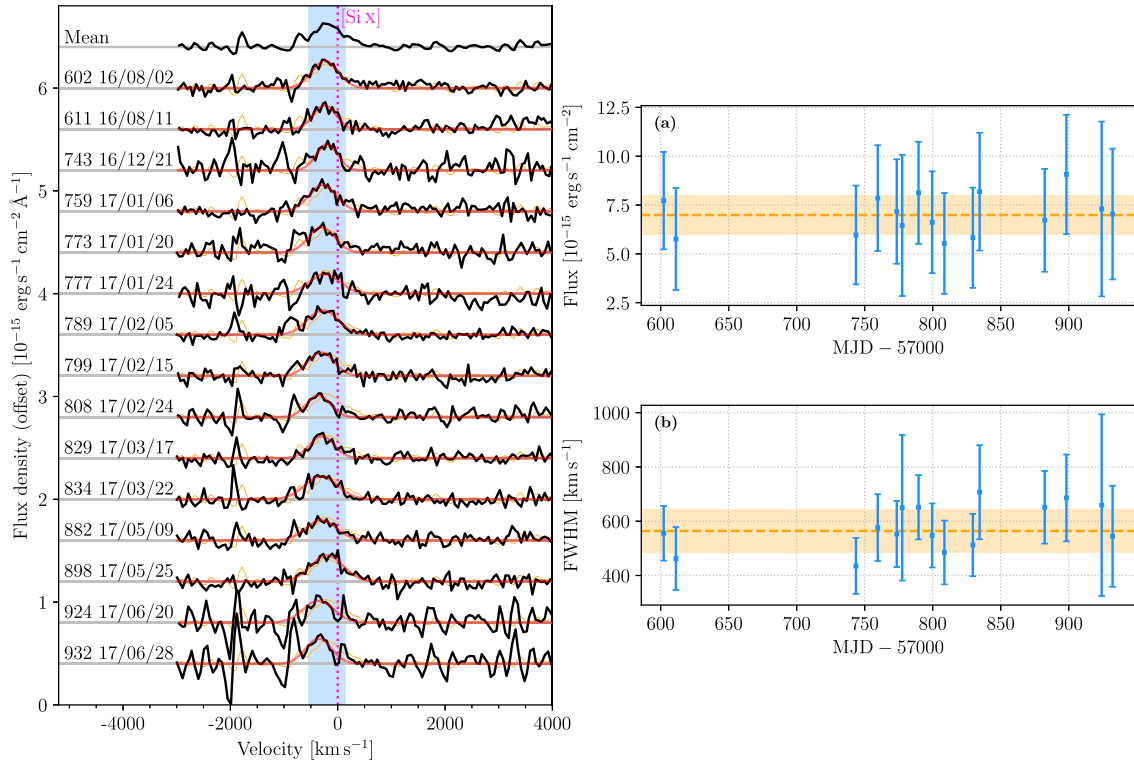


**Figure 9.** The [Si x] coronal line in the mean and single-epoch spectra. Description as in Fig. 5.

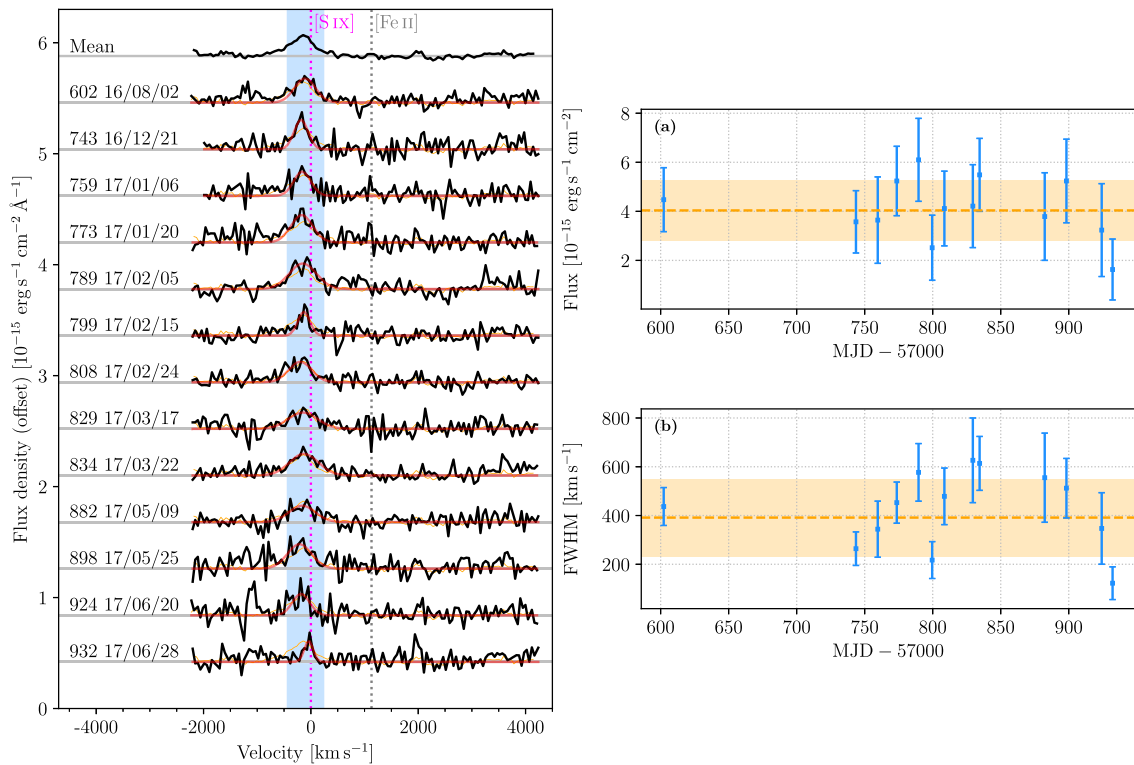


**Figure 10.** The [S IX] coronal line in the mean and single-epoch spectra. Description as in Fig. 5.

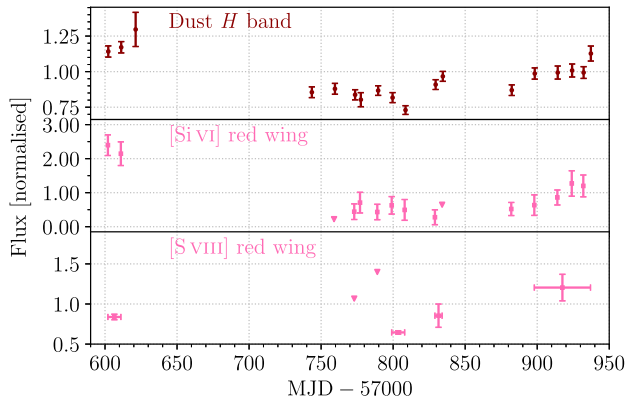


**Figure 11.** Top: The  $H$  band (1.55–1.60  $\mu\text{m}$ ) dust flux, from Landt et al. (2019). Middle and bottom: The [Si VI] and [S VIII] broad red wing fluxes, from this work. We have binned [S VIII] measurements from consecutive epochs and plot the error-weighted averages and standard deviations. All fluxes are normalised to their mean value.

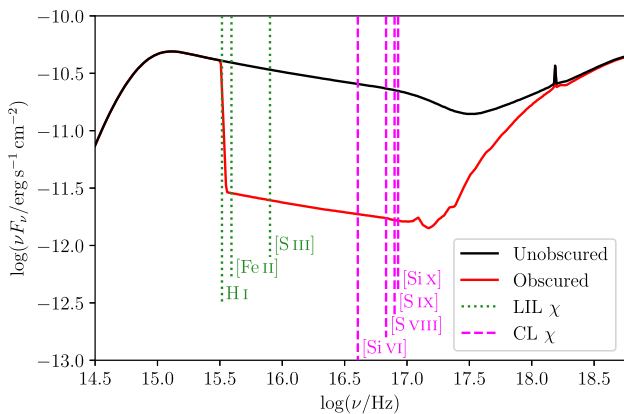


**Figure 12.** The unobscured and obscured SEDs of NGC 5548 (Mehdipour et al. 2015) are shown as solid black and red lines, respectively. Dotted green lines indicate the ionization potentials ( $\chi$ ) of the low-ionization lines (LIL) H I, [Fe II], and [S III]. Dashed magenta lines show the ionization potentials of the coronal lines (CL), ranging from 166.8 eV for [Si VI] to 351.1 eV for [Si X] (see Table 1).

does impact on the low-ionization lines. It is worth mentioning that tests have shown that the cloud can be highly ionized in some cases. In such cases, the temperature at the illuminated face of the cloud gets very high ( $>10^6$  K in some cases), resulting in almost no near-IR and UV high-ionization lines being produced at the illuminated face. In those cases, the EWs of all coronal lines will significantly change by varying the column density.

Fig. 13 shows the results for the models with  $\log(N_{\text{H}}/\text{cm}^{-2}) = 23$ . The obscured case is shown in plots 13(a) and (b), and the unobscured case is shown in plots (c) and (d). Plots (a) and (c) illustrate how the EW of each near-IR coronal line (and also [S III]) depends on the location (vertical axis) and the hydrogen density (horizontal axis) of the cloud. The lower-right-hand panel in these plots shows the contours for [S VIII] and [Si VI] overlaid. Plots (b) and (d) show the contours for the optical coronal lines ([Fe VII]  $\lambda 3759$ , [Fe X]  $\lambda 6374$ , and [Fe XI]  $\lambda 7892$ ). The lower-right hand panels of this series of plots have been created using the approach introduced by Dehghanian et al. (2020). In these panels, each coloured line shows the observed value of one specific coronal line. By tracing these lines, one might be able to find the place where they (almost) cross over each other. The

crossover point would indicate the location and the density of the cloud that produces the observed line strengths.

## 5.2 Solution for the coronal line cores

Considering Fig. 13, we ran over a hundred location-density points for three column densities of  $\log(N_{\text{H}}/\text{cm}^{-2}) = 22, 22.5, \text{ and } 23$ . Tables 5 and 6 show some of the results from the mentioned CLOUDY simulations. We mainly selected those clouds that produce zero to one hundred per cent of near-IR coronal lines within a reasonable range of uncertainty (a tolerance of  $\approx 30$  per cent). Models 3 and 5 overproduce [S VIII] beyond this uncertainty, but are still presented in the table since they produce the right amount of [Si VI].

Regarding the optical coronal lines ([Fe II], [Fe VII], and [Fe X]), as explained in Section 5.1, since we lack contemporaneous measures of these lines we search for models that agree with the observed values to within a factor  $\approx 2$ –3.

As both tables indicate, there is not a single location-density solution for which the cloud produces all of the observed coronal lines, implying that we must be seeing emission from different regions. By comparing the models, we note that while [S VIII] and [Si VI] are produced by the same cloud, [S IX] and [Si X] are emitted by different cloud(s). Also, since we could find more solutions in the obscured case, it is most likely that the coronal line regions saw the photonionising source through the obscurer during this near-IR spectroscopic campaign. However, it is also possible that the continuum source was unobscured to some coronal line production sites (i.e. the coronal line gas was located between the obscurer and the source), but obscured at other locations (i.e. the gas was located between the obscurer and the observer). The CLOUDY simulations indicate that models 3 (or 5) and 7 are most likely responsible for producing the observed values of the near-IR coronal line cores. In this scenario, cloud 7 produces almost all of the [Si X], while cloud 3 (or 5) produces [S VIII], [S IX], and [Si VI]. Model 4 is also a good choice to produce the right amount of [S VIII] and [Si VI], however this cloud does not produce enough [S IX].

In general, it is difficult to produce sufficient [Si X] emission without underestimating the emission from the other near-IR coronal lines. Furthermore, the [Si X] region requires on average a gas density reduced by a factor of  $\sim 1000$  (and a somewhat larger distance from the central continuum source).

## 5.3 Solution for the coronal line wings

The values listed in Tables 5 and 6 are fluxes relative to the mean flux of the narrow emission line cores. In our mean spectrum, the wings of [S VIII] and [Si VI] are  $62 \pm 11$  and  $95 \pm 7$  per cent of the core fluxes, respectively. The ideal model to explain the coronal line wings will therefore produce a flux in [S VIII] equivalent to  $\approx 62$  per cent of its core flux, a flux in [Si VI] equivalent to  $\approx 95$  per cent of its core flux, and 0 per cent of the core flux of all of the other lines (none of which display wings). For the unobscured SED, we find a solution (model 8, Table 6) at a radius  $\log(R/\text{cm}) = 17.25$  that produces fluxes in [Si VI] and [S VIII] that are very similar to the observed fluxes in the broad wings of these lines. The model predicts a flux equivalent to 94 per cent of the narrow core flux of [Si VI] will be produced at this location (precisely what we measure for the flux in the wings in the mean spectrum). It also predicts an equivalent of 92 per cent of the [S VIII] flux will be produced here (an overprediction, since we measure 62 per cent). Furthermore, no [Si X] and very little [S IX] emission (equivalent to 3 per cent of the core flux) are produced in this region. Model 8 is therefore a near-ideal solution for the coronal

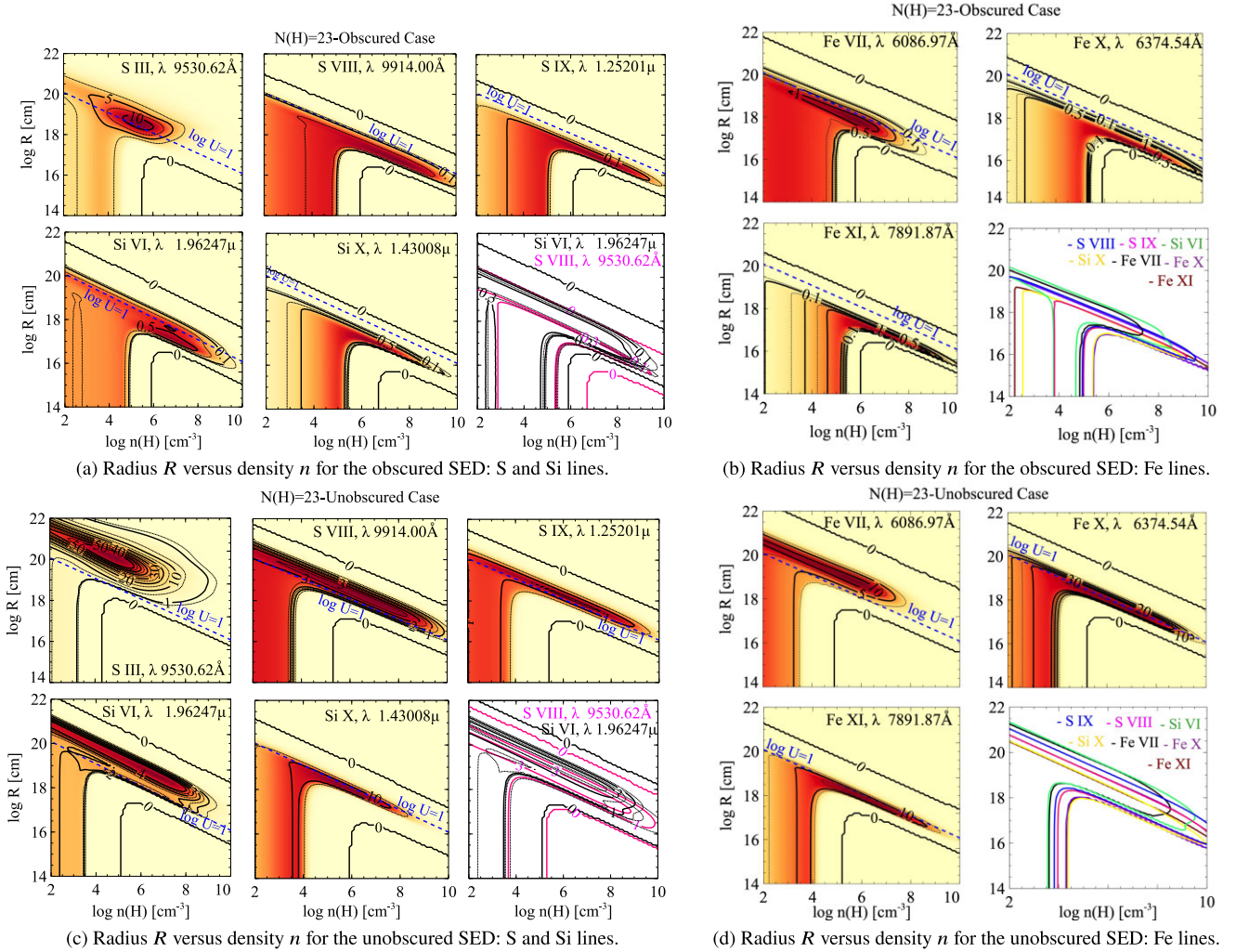


**Figure 13.** CLOUDY simulations for the four near-IR coronal lines, three optical coronal lines and [S III]  $\lambda$  9530. Plots (a) and (c) (plots [b] and [d]) show the radius and density of the S and Si (Fe) line-emitting gas. Contours trace the equivalent widths (EWs) of the emission lines with respect to the continuum at 1215 Å. The blue dashed line shows the ionization parameter  $\log U = 1$  in the parameter space. Plots (a) and (b) have been calculated using the obscured SED; plots (c) and (d) using the unobscured SED. The bottom right-hand panels in plots (a) and (c) show an overlay of the contours for [S VIII] and [Si VI] (the two coronal lines which exhibit wings) for easier comparison. The bottom right-hand panels in plots (b) and (d) show the EW contours corresponding to the observed fluxes of the optical coronal lines in a single panel.

**Table 5.** A comparison of CLOUDY coronal line flux predictions to the observed values in the obscured case.

Coronal line	Model 1 $N_{\text{H}} = 10^{23}$ $R = 10^{17.3}$ $n_{\text{H}} = 10^{7.4}$	Model 2 $N_{\text{H}} = 10^{22}$ $R = 10^{16.3}$ $n_{\text{H}} = 10^8$	Model 3 $N_{\text{H}} = 10^{22.5}$ $R = 10^{16.6}$ $n_{\text{H}} = 10^{8.3}$	Model 4 $N_{\text{H}} = 10^{22.5}$ $R = 10^{16.7}$ $n_{\text{H}} = 10^{8.3}$	Model 5 $N_{\text{H}} = 10^{22.5}$ $R = 10^{16.6}$ $n_{\text{H}} = 10^{8.2}$	Model 6 $N_{\text{H}} = 10^{23}$ $R = 10^{17.6}$ $n_{\text{H}} = 10^{7.5}$	Model 7 $N_{\text{H}} = 10^{22}$ $R = 10^{18}$ $n_{\text{H}} = 10^{4.5}$	
(1)	(2)	(3)	(4)	(5)	(6)	(7)	(8)	
[S VIII]	0.9914 $\mu\text{m}$	70 %	<1 %	151 %	118 %	167 %	3 %	<1 %
[S IX]	1.2520 $\mu\text{m}$	7 %	2 %	46 %	23 %	64 %	<1 %	4 %
[Si VI]	1.9625 $\mu\text{m}$	129 %	0 %	81 %	79 %	90 %	58 %	<1 %
[Si X]	1.4300 $\mu\text{m}$	<1 %	39 %	5 %	2 %	12 %	0 %	81 %
[Fe VII]	3759 Å	78 %	<1 %	19 %	18 %	23 %	20 %	<1 %
[Fe X]	6374 Å	23 %	97 %	188 %	77 %	309 %	<1 %	212 %
[Fe XI]	7892 Å	<1 %	81 %	10 %	3 %	20 %	<1 %	167 %

*Note.* The columns are: (1) Ion and wavelength of the near-infrared transition; (2)–(8) the percentage of the observed flux predicted by different CLOUDY models. For [S VIII] and [Si VI] the percentages are relative to the line core fluxes (excluding the wings).

**Table 6.** A comparison of CLOUDY coronal line flux predictions to the observed values in the unobscured case.

Coronal line	Model 8 $N_{\text{H}} = 10^{23}$ $R = 10^{17.25}$ $n_{\text{H}} = 10^{9.5}$	Model 9 $N_{\text{H}} = 10^{23}$ $R = 10^{16.2}$ $n_{\text{H}} = 10^{4.4}$	Model 10 $N_{\text{H}} = 10^{23}$ $R = 10^{17.55}$ $n_{\text{H}} = 10^{6.3}$	
(1)	(2)	(3)	(4)	
[S VIII]	0.9914 $\mu\text{m}$	92 %	0 %	<1 %
[S IX]	1.2520 $\mu\text{m}$	3 %	<1 %	<1 %
[Si VI]	1.9625 $\mu\text{m}$	94 %	0 %	0 %
[Si X]	1.4300 $\mu\text{m}$	0 %	58 %	110 %
[Fe VII]	3759 $\text{\AA}$	8 %	0 %	0 %
[Fe X]	6374 $\text{\AA}$	3 %	5 %	10 %
[Fe XI]	7892 $\text{\AA}$	<1 %	13 %	35 %

*Note.* The columns are: (1) Ion and wavelength of the near-infrared transition; (2)–(4) the percentage of the observed flux predicted by different CLOUDY models. For [S VIII] and [Si VI] the percentages are relative to the line core fluxes (excluding the wings).

line wings. Model 1 in the obscured case (Table 5) has some similar properties to model 8: it is at a similar radius ( $\log [R/\text{cm}] = 17.3$ ), and produces substantial [S VIII] and [Si VI] emission, with little [S IX] and [Si X]. However, more Fe coronal line emission is produced in this model compared with model 8:  $\approx 78$  per cent of the observed [Fe VII]  $\lambda 3759$  and  $\approx 23$  per cent of the observed [Fe X]. Interestingly, the radius of both of these coronal line emitting clouds  $\log (R/\text{cm}) \approx 17.3$  or 70 light-days, which is exactly the radius of the inner torus as determined from the hot dust reverberation lags by Landt et al. (2019). However, the coronal line gas density in the unobscured case is similar to what is expected for the dusty torus material, whereas it is a factor of  $\sim 100$  lower in the obscured case. We discuss this case further in Section 6.2.

## 6 DISCUSSION

We have performed an in-depth study of the near-IR coronal lines in NGC 5548, making use of spectroscopic data recorded over a year with a roughly weekly cadence. We were able to study not only the line profile shapes but the changes in line shapes and fluxes. We have shown that two of the coronal lines ([S VIII] and [Si VI]) have prominent broad wings as well as narrow cores, whereas only narrow cores are evident on the other two coronal lines. Whilst the narrow line cores are persistent and clearly detected in all spectra, the wings are highly variable; the flux in the wings is comparable to the flux in the line cores in some epochs, and in other epochs the wings are barely visible. In the case of [Si VI], it is clear that most of the variability in the line profile is in the wings. Broadly speaking, there must be at least two coronal line regions in NGC 5548: one that produces the persistent, narrow cores of all four coronal lines and another (presumably more compact) region in which the conditions favour the production of [S VIII] and [Si VI] emission which we observe as the broad, variable wings.

The existence of multiple sites of coronal line emission in AGN has been proposed before based on comparisons between Seyfert type 1 and type 2, but never before shown for a single object. Murayama & Taniguchi (1998) reported excess [Fe VII]  $\lambda 6087$  emission in Seyfert 1 nuclei compared with Seyfert 2s, implying that some coronal line emission occurs interior to the dust torus (and so can be seen only in Seyfert 1s) and some coronal line emission occurs beyond the torus. They proposed three main coronal line regions: the inner face of the dust torus, highly ionized clumps of gas in the NLR, and a further,

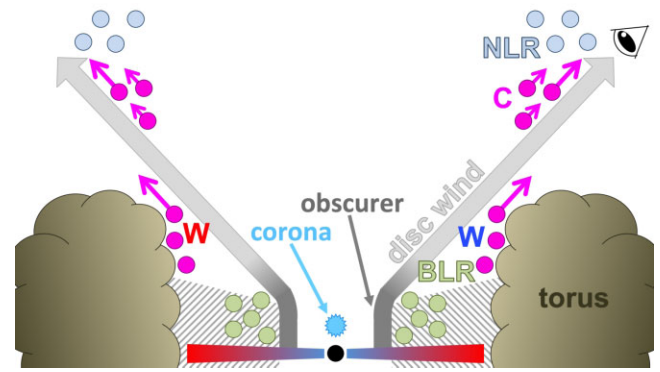


**Figure 14.** A cartoon of the possible geometry of the nucleus in NGC 5548. A wind (Dehghanian et al. 2019) is launched from the disc: its dense base (the ‘obscurer’ in dark grey) partly shadows the BLR (light green clouds). The less dense streamlines of the wind (light grey) extend to large distances. Gas producing the narrow cores of the coronal lines (magenta clouds labelled ‘C’) is located just inside of the standard NLR (light blue clouds). The outflowing coronal line gas may be accelerating, as indicated by the magenta arrows. The blue and red wings seen on the [S VIII] and [Si VI] coronal lines (marked with the blue and red ‘W’, respectively) may be produced on the inner face of the torus. The torus may partially block our view of the gas producing the blue wing.

very extended region on kpc scales. We take up this interpretation for the coronal line regions in NGC 5548 in more detail below and sketch it in Fig. 14.

### 6.1 The coronal line cores

In Section 3.1, we carefully analysed the emission line profiles in the high S/N mean spectrum. In addition to the four near-infrared coronal lines, we also measured the low-ionization forbidden line [S III]  $\lambda 9531$ . In comparison to [S III], the cores of all four coronal lines are broader (ranging from FWHM  $\approx 550$ – $750 \text{ km s}^{-1}$ ) and are blueshifted with respect to it by  $\approx 120$ – $380 \text{ km s}^{-1}$  (Fig. 3). The greater widths and blueshifts of the coronal lines with respect to the low-ionization forbidden lines are commonly seen in AGN spectra and were reported in early studies (e.g. Grandi 1978; Pelat, Alloin & Fosbury 1981). This implies that the coronal lines are produced in different gas to the standard NLR responsible for the emission from low-ionization species such as [S III] and [O III]. This is consistent with the idea that the coronal line emitting gas is part of an outflowing wind on scales more compact than the standard NLR. Our measurements of the coronal line cores over the duration of the campaign indicate that they are only weakly variable, if at all. In Section 4.2.3, we noted a positive relationship between the FWHM and flux over time in the single-epoch measurements of the line cores. This trend (if real) could be explained if the gas producing the broadest part of the line profiles is more compact (and varies more rapidly) than the gas producing the more persistent narrow cores of the lines. However, in our data, the same FWHM-flux trend can alternatively be explained by the movement of the underlying continuum within its uncertainty range, so we cannot draw any strong conclusion on this point. In any case, the weakness of the variability is consistent with a geometry in which the majority of the flux in the coronal line cores is emitted at radii  $\gtrsim 1$  light-year and therefore the line cores have a variability time-scale longer than we can probe with this data. Then, considering both the profile widths and variability properties, we may deduce that the coronal line cores are produced

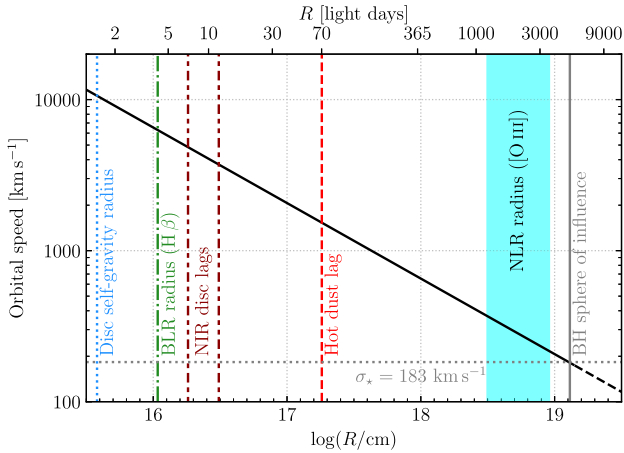


**Figure 15.** Orbital velocity as a function of radius for a black hole of mass  $3.2 \times 10^7 M_{\odot}$ . The black hole’s sphere of influence extends up to  $\log(R/\text{cm}) \approx 19.1$ . We indicate radii of the  $H\beta$  BLR (green: Pei et al. 2017); hot dust (red: Landt et al. 2019); and [O III] NLR (cyan: Peterson et al. 2013).  $H$  and  $K$  band lags attributed to the outer accretion disc (dark red: Landt et al. 2019) suggest that the disc extends beyond its self-gravity radius (blue: Gardner & Done 2017). The X-ray obscurer (the base of a disc wind) must be interior to the BLR (Dehghanian et al. 2019). The stellar velocity dispersion of the bulge was measured to be  $\sigma_* = 183 \text{ km s}^{-1}$  (Ferrarese et al. 2001).

at a characteristic radius  $18 \lesssim \log(R/\text{cm}) \lesssim 18.5$  from the nucleus, a scale intermediate between the BLR and NLR (Fig. 15).

Although the widths and shifts of the four coronal line cores have common characteristics (being broader and blueshifted with respect to [S III]), they are not identical. It is likely that the lines are not emitted entirely cospatially and different coronal lines originate in different parts of the outflow. Our photoionization simulations with CLOUDY (Section 5) also strongly suggest this, since we do not find any single cloud that can account for all of the observed lines. In the mean spectrum, [S IX] was found to be the narrowest coronal line ( $\text{FWHM} = 554 \pm 24 \text{ km s}^{-1}$ ) and [S VIII] the broadest ( $\text{FWHM} = 737 \pm 39 \text{ km s}^{-1}$ ). Consistent with previous studies (e.g. Pelat et al. 1981; Filippenko & Halpern 1984; Penston et al. 1984; De Robertis & Osterbrock 1986; Ferguson et al. 1997; Rodríguez-Ardila et al. 2011), we found a trend of increasing FWHM with the ionization potential of forbidden emission lines (Fig. 4).<sup>2</sup> Rodríguez-Ardila et al. (2011) noted that this trend extended up to  $\chi \approx 300 \text{ eV}$ , above which the FWHM of lines decreased or plateaued, which is what we observe in Fig. 4: [Si X] ( $\chi = 351.1 \text{ eV}$ ) is no broader than [S VIII] ( $\chi = 281.0 \text{ eV}$ ) and [S IX] ( $\chi = 328.8 \text{ eV}$ ) is narrower than [S VIII]. Since [S VIII] has the highest critical density of the lines studied here, some of its emission may arise from higher density gas nearer to the nucleus where orbital motions are greater. In this picture, it is therefore expected that [S VIII] will be the broadest coronal line, as we observe. This result suggests a degree of stratification of the coronal line emitting gas.

Pelat et al. (1981) found a relationship between line width and ionization potential, as well as line width and velocity shift, with the general trend that higher-ionization lines were broader and more strongly blueshifted. We see such a trend to first order (the coronal lines are broader than, and blueshifted with respect to, [S III]); however, the reverse trend is seen within the coronal line sequence:

the lowest-ionization coronal line [Si VI] has the greatest blueshift (Fig. 4). The [S VIII], [S IX], and [Si X] lines have centroid shifts that are consistent within error, with a mean and standard deviation of  $-125$  and  $9 \text{ km s}^{-1}$ , respectively; the [Si VI] line has a significantly greater shift of  $-383 \pm 10 \text{ km s}^{-1}$ . This difference in blueshifts is real, and not the result of a systematic error in the wavelength calibration at the red end of our spectra: we assessed the centroid shifts of the low-ionization [Fe II]  $1.644 \mu\text{m}$  line near to [Si VI] and did not find any significant shift of this line. Therefore, the kinematics of the [Si VI]-emitting gas appear to be different to that of gas emitting the other three coronal lines. Ferguson et al. (1997) noted that their photoionization models predicted that lower-ionization coronal lines ([Ne V]–[Si VII]) would form in more extended gas than the high-ionization lines. We see this trend in our CLOUDY simulations, in which the contours of [Si VI] are displaced to larger radii compared with the other coronal lines (see the comparison of [S VIII] and [Si VI] contours in Fig. 13). We also find that the core of the [Si VI] line is narrower than that of [S VIII] and [Si X], which (if interpreting the line widths as orbital motion) would also imply its emission occurs at typically larger radii. If the [Si VI]-emitting gas is located at larger radii and greater velocities than the rest of the coronal line gas, this implies that the gas is part of an accelerating outflow. Outflows which accelerate from the nucleus to distances of  $\sim 100 \text{ pc}$  have been observed in several other AGN (e.g. Crenshaw et al. 2000; Crenshaw & Kraemer 2000; Müller-Sánchez et al. 2011).

Our photoionization simulations appear to predict a very compact origin for the coronal line cores (Section 5.2). CLOUDY models 3 or 5 produce approximately the same fluxes as we observe in the cores of the [S VIII], [Si X], and [Si VI] lines, and the location of the line-emitting gas in these solutions is  $\log(R/\text{cm}) = 16.6$ , a similar scale to the BLR or outer accretion disc (see Fig. 15). The widths of the lines do not necessarily reflect Doppler broadening by virial motion of the emitting gas; instead, the lines may be broadened by gas turbulence, as is the case in coronal line novae. However, the blueshifts of the coronal lines strongly suggest that the emitting gas is outflowing. It is then reasonable to assume that the outflow is launched from the rotating accretion disc. In this case, we would expect the gas to have a large amount of rotational as well as radial motion, and for this to be evident in the widths of the emission lines.

The CLOUDY simulations also suggest that the three coronal lines [S VIII], [S IX], and [Si VI] may be produced in the same cloud (either 3 or 5), and [Si X] is produced in another cloud (7). However, the most obvious difference in the coronal line core profiles is the much greater blueshift of [Si VI] with respect to the other lines. This suggests that [Si VI] emitting gas is kinematically (and spatially) distinct from the gas producing the other three coronal lines, or alternatively, has an additional component not seen in the other lines, which would not be accounted for in our CLOUDY solutions.

Landt et al. (2015b) determined greater distances for the coronal line gas in NGC 5548 than implied here. Based on measurements of the optical and X-ray coronal lines, they calculated that the coronal lines were produced in a low-density gas ( $\log[n_e/\text{cm}^{-3}] \sim 3$ ) at  $\log(R/\text{cm}) \approx 18.9$  ( $\approx 8$  light-years). This distance is approximately coincident with the [O III]  $\lambda 5007$  NLR and is just within the black hole’s gravitational sphere of influence (see Fig. 15). In spite of the similar size scale to the NLR, Landt et al. (2015b) proposed that the coronal line region was likely to be an independent entity because of its high ionization parameter ( $U \sim 1$ ). The modest variability of the coronal line cores and their relatively narrow widths imply their origin in gas interior to the standard NLR ( $\log[R/\text{cm}] \lesssim 18$ ). The photoionization simulations in Section 5.2 suggest an even more compact coronal line region at  $\log(R/\text{cm}) = 16.6$ . It can be seen

<sup>2</sup>Contrary to Filippenko & Halpern (1984), we observe a weaker relationship between emission line FWHM and critical density, as can be seen in Fig. 4.

from Tables 5 and 6 that CLOUDY generally predicts much higher gas densities ( $\log [n_{\text{H}}/\text{cm}^{-3}] \sim 7\text{--}9$ ) than calculated by Landt et al. (2015b). Our results are not necessarily at odds with those of Landt et al. (2015b) since they derived physical parameters from optical and X-ray coronal lines, whereas we do so for the near-IR coronal lines. Since emission lines form wherever the conditions allow them to do so, it is likely that different coronal lines trace clumps of differing density, thus mapping out the outflowing wind that produces them.

In summary, the kinematics inferred from the narrow line profile widths suggest that the coronal line cores are emitted in an accelerating wind just interior to the low-ionization NLR. However, at odds with this interpretation, we did not find photoionization model solutions consistent with it, although there are a number of limitations to this modelling, as mentioned earlier. Therefore, it is possible that the line widths are not produced by virial motion within the black hole's gravitational field, but rather indicate radial motion as in the ejecta of classical novae during their coronal line phase (e.g. Greenhouse et al. 1990; Woodward et al. 2021).

## 6.2 The coronal line wings

Before proceeding, it is worth considering whether the flux excesses seen near [Si VI] and [S VIII] (their 'wings'), and the apparent variability of these features, could alternatively be explained by other spectral components unrelated to the coronal lines (i.e. the continuum or the blended broad emission lines). We have incorporated the uncertainty on the placement of the continuum (assumed to be locally linear) in our flux measurements, and the variability of the excess flux redward of [Si VI] is still highly significant; therefore, we can rule out the excess flux changes being due to the imperfect subtraction of a (smooth) continuum. Of course, the shapes of these flux excesses do not look like parts of a smooth continuum, and it does not seem likely that the variations could be due to variations in unexplained, local features in the continuum, either. As the spectral decomposition by Landt et al. (2019) showed, the continuum beneath [S VIII] 0.9914  $\mu\text{m}$  is dominated by the accretion disc, whereas the continuum beneath [Si VI] 1.9650  $\mu\text{m}$  is dominated by emission from the hot dust. So, even if it were the case that the wings are in fact continuum features, this interpretation requires there to be some physical link between the disc and dust emission at the *specific* wavelengths 0.9914 and 1.9650  $\mu\text{m}$ , respectively, which creates the similarly shaped and similarly varying flux excesses. So, we do not think it likely that the appearance and variability of these features can be attributed to the dust or disc continua.

The other possibility is that these spectral and temporal features are caused by the imperfect deblending of the coronal lines from the broad emission lines. We used the mean Pa  $\beta$  profile as a (scaled) template for all of the broad hydrogen lines in our extraction of the coronal line profiles from the single-epoch spectra (Section 3.2). Therefore, any deviations of the broad lines from the average profile shape can cause features in the residuals which we may attribute to the coronal lines. In the case of [Si VI], such an effect is likely to be relatively minor. Our spectral decomposition of the high-S/N mean spectrum around that line (Fig. 2) indicates that Br  $\delta$  and particularly Pa  $\alpha$  are very weak features beneath [Si VI]. The flux in Br  $\delta$  beneath the [Si VI] red wing is  $\approx 6 \times 10^{-15} \text{ erg s}^{-1} \text{ cm}^{-2}$ , less than the average flux in the red wing itself ( $8.7 \times 10^{-15} \text{ erg s}^{-1} \text{ cm}^{-2}$ ). The flux variations we attribute to the [Si VI] red wing are of the order  $10 \times 10^{-15} \text{ erg s}^{-1} \text{ cm}^{-2}$ . So, if this variability were actually dominated by variations in Br  $\delta$  it would require incredibly large changes in the red wing of Br  $\delta$ . We would then expect to see concomitant changes in the other broad hydrogen line profiles, which

we do not. So it appears that both Br  $\delta$  and Pa  $\alpha$  are too weak in this part of the spectrum to satisfactorily explain the changes we see in the flux excess. Relatively minor changes in the broad Pa  $\delta$  profile could more plausibly induce a feature that we mistake for [S VIII] emission. But, in this interpretation, it is then a coincidence that this flux excess on the blue shoulder of Pa  $\delta$  appears at just the right location to give the appearance of a red wing on [S VIII], with a similar shape and scale to the excess around [Si VI] (which sits on the red wing of Br  $\delta$ ). Additionally, if our deblending method did not generally work well, it is curious that we do not observe any excess flux around [S IX] (which is blended with broad Pa  $\beta$ ). This similarity in the profile shapes and light curves of the [S VIII] and [Si VI] wings actually strengthens our preferred interpretation of these flux excesses as coronal line emission, since our CLOUDY simulations demonstrate that emission from both [S VIII] and [Si VI] can be produced by the same gas cloud, on  $\sim$ light-month scales from the nucleus. We therefore conclude that the observed excess emission around the [S VIII] and [Si VI] lines (and the variability of these features) is genuinely associated with those lines.

It is then intriguing that we see broad wings on two of the near-IR coronal lines ([S VIII] and [Si VI]) but not on the other two ([S IX] and [Si X]). Since we observe wings on one sulphur and one silicon line, the absence of wings on some lines cannot simply be related to the absence of that element at that location (for example, if silicon were depleted on to dust). Our CLOUDY models show that the appearance of these wings may be explained by photoionization: we observe wings on the two coronal lines with the lowest ionization potentials simply due to the combination of bolometric luminosity of the central source and the gas density of the coronal line emitting gas. Models 8 and 1, which we described in Section 5.3, are appealing because they explain a number of observed properties. CLOUDY predicts emission from [Si VI] and [S VIII] emission at similar fluxes to those we observe in the wings occurring at  $\log (R/\text{cm}) \approx 17.3$ . Additionally, very little [S IX] and [Si X] emission is produced at this location, explaining the absence of wings on these two lines. In model 8 none of the other lines we have assessed ([S III] or the optical Fe coronal lines) are strongly emitted, either. Since we observe strong variability in the wings as they disappear and reappear over the year-long campaign, we can infer that the emission must arise on  $\sim$ light month scales; the radius  $\log (R/\text{cm}) \approx 17.3$  equates to  $\approx 70$  light-days so the implied spatial scale is consistent with the observed variability time-scale. As can be seen in Fig. 15, orbital motions of a few thousand  $\text{km s}^{-1}$  are expected at this radius, which would explain the observed extents of the wings in velocity. A value of 70 light-days is also the precise radius of the inner edge of the torus determined by Landt et al. (2019) via the reverberation of the dust in response to the optical accretion disc emission. The strong similarity in the shapes of the [Si VI] wing and hot dust light curves (Fig. 11) means that the two will have similar reverberation lags and so it is likely that the hot dust and coronal line wings are emitted at the same radius from the nucleus.

It is clear from Figs 3 and 8 that the broad coronal line wings are much more prominent on the red side of the core than on the blue side. If the wings are indeed produced in a wind launched off the inner edge of the torus, then the torus may be inclined such that our view of the approaching gas is blocked, and we see mostly the receding gas on its far side (see Fig. 14). A similar geometry was also proposed by Glidden et al. (2016) to explain observations of coronal line forest AGN (see their figure 1). Pier & Voit (1995) proposed that AGN coronal line emission would originate in an X-ray heated wind evaporated from the inner edge of the dust torus, and this was one of the main sites of coronal line production outlined by Murayama & Taniguchi (1998). Our findings are consistent with

these schemes. However, our chosen model is problematic in that the torus must see the unobscured SED, yet the obscurer is located between the torus and the X-ray source (see e.g. figure 4 of Kaastra et al. 2014). A possible solution is that, if the obscurer is an extended stream or wind, it presents a much higher column density along our line of sight than toward the torus. In any case, the torus emission is not sensitive to the obscurer since it is heated mainly by the UV/optical nuclear emission and the obscurer is transparent at these wavelengths (Dehghanian et al. 2019). But the coronal lines can very well differentiate between the obscured and unobscured SED through constraints on the gas density. The value of  $\log(n_{\text{H}}/\text{cm}^{-3}) \sim 9$  in the unobscured case (model 8) is what is expected of the material in the dusty torus.

Whilst the shapes of the [Si VI] wing and hot dust light curves are strikingly similar (Fig. 11), it is noteworthy that the amplitude of the [Si VI] wing variability is substantially greater than that of the dust. The wing varies by more than an order of magnitude whereas the dust flux variations are only at the  $\pm 25$  per cent level. Stronger variability of the coronal lines in NGC 5548 compared with the dust on time-scales of several years was also reported by Landt et al. (2015b). This behaviour is expected if the coronal line wing emission varies mainly in dependence on the compact X-ray source, which in turn varies with a higher amplitude and on shorter time-scales than the UV/optical emission that heats the dust (Edelson et al. 2015).

Both our spectroscopic analysis and photoionization models point to the inner face of the torus being the origin of the coronal line wings. But we stress that we cannot claim that our CLOUDY models present unique and definitive solutions and there are several caveats to bear in mind, such as, e.g. the assumption of particular SEDs non-contemporaneous with our emission line observations and the inexhaustive exploration of the parameter space. Nonetheless, these models serve to illustrate that our proposed solution for the origin of the coronal line wings is physically plausible.

### 6.3 Links to outflowing absorption systems

We interpreted the blueshifts of the coronal line cores as evidence of emission from outflowing gas. Outflows in NGC 5548 have been detected via absorption lines in other wavebands, including X-rays (Ebrero et al. 2016), UV (Arav et al. 2015), and near-IR (Wildy et al. 2021). Some of the X-ray warm absorber components in NGC 5548 are related to the UV absorbers (e.g. Arav et al. 2015; Ebrero et al. 2016) and Wildy et al. (2021) associated several narrow He I 1.08  $\mu\text{m}$  absorption features with corresponding UV absorbers. Similarities between the inferred properties of the coronal line region and warm absorber (both are thought to originate in a highly ionized, outflowing gas on scales intermediate between the BLR and NLR) have prompted further investigation into the possibility that they are in fact the same medium. Porquet et al. (1999) used photoionization models to demonstrate that coronal emission lines could indeed form within the warm absorber. They found that very high gas densities ( $\log[n_{\text{H}}/\text{cm}^{-3}] \gtrsim 10$ ) were required to avoid overproduction of the coronal lines relative to observations and that the gas was located on scales similar to the BLR. It is therefore pertinent to investigate whether the near-IR emission features seen in the outflow of NGC 5548 (i.e. the coronal lines) can be associated with the gas responsible for the observed absorption features.

The associations of X-ray, UV, and near-IR absorption features were based on the gaseous kinematics (i.e. similar velocity shifts), with further consideration made of the gas properties (density, ionization parameter). The velocity shifts we determined for the coronal lines ( $\approx -125 \text{ km s}^{-1}$  for [S VIII], [S IX], and [Si X];  $\approx -380 \text{ km s}^{-1}$

for [Si VI]) do not closely match those reported for any of the absorption features mentioned above. Additionally, the majority of these absorption features arise at much greater distances from the nucleus than we infer for the coronal lines. The estimated location of the UV absorption clouds is at the NLR radius and above ( $\gtrsim 2 \text{ pc}$  or  $\log[R/\text{cm}] \gtrsim 18.8$ ), whereas the coronal lines are likely to be produced interior to the NLR. The highest-ionization components of the X-ray warm absorber are located on smaller scales ( $\log[R/\text{cm}] \gtrsim 18$ ), similar to what we infer for the coronal lines, although these components have much higher outflow velocities (blueshifts of  $\approx 250\text{--}1200 \text{ km s}^{-1}$ ) and much narrower widths ( $\sigma_v \approx 20\text{--}200 \text{ km s}^{-1}$ ) than we observe in the coronal lines. Our photoionization modelling with CLOUDY suggests that the coronal lines observed in NGC 5548 form in gas of densities  $\log(n_{\text{H}}/\text{cm}^{-3}) \sim 7\text{--}9$ , much lower density than the  $\log(n_{\text{H}}/\text{cm}^{-3}) \gtrsim 10$  required by Porquet et al. (1999), but also much higher than the range of densities calculated for the warm absorber in NGC 5548 ( $\log[n_{\text{H}}/\text{cm}^{-3}] \sim 3\text{--}5$ ; Ebrero et al. 2016).

In summary, although the outflow velocities of the coronal line gas are of the same order of magnitude as those of some of the observed absorbers ( $\sim$ few hundred  $\text{km s}^{-1}$ ), we see little evidence of an association between the coronal line gas and the specific X-ray/UV absorption components previously reported in NGC 5548. Then, if the coronal line gas and the absorbers are indeed parts of the same wind, they must arise from widely different clumps and so are unlikely to be exactly cospatial.

## 7 SUMMARY AND CONCLUSIONS

We have performed the first intensive study of the variability of the near-infrared coronal lines in an AGN. The near-infrared spectroscopic monitoring campaign of Landt et al. (2019) reveals a complex and multicomponent coronal line region. From measurements of the high-S/N mean spectrum of the campaign, we observe some general trends that have been observed in previous studies of AGN coronal lines. The narrow cores of the coronal lines are broader than, and blueshifted with respect to, the lower-ionization forbidden lines. The lack of strong variability of the coronal line cores in the year-long campaign suggests the majority of the line-emitting gas exists on scales  $\gtrsim 1$  light-year, whilst the line widths suggest the gas is more compact than the standard NLR ( $\lesssim 3$  light-years). These findings suggest that the narrow near-IR coronal lines in NGC 5548 form in an outflow just interior to the inner NLR, although our photoionization models show that coronal line emission originating closer to the BLR is possible. An approximate correlation between the FWHM and ionization potential of the coronal line cores implies a stratification of line emitting gas, with the lowest-ionization coronal line [Si VI] line forming at a greater distance from the nucleus than the other lines. The greater blueshift and narrower line profile of [Si VI] with respect to the higher-ionization lines [S VIII] and [Si X] can be understood if this stratified wind is accelerating. We therefore propose that the narrow coronal line cores form in a stratified, accelerating outflow from the nucleus of NGC 5548 and that this emission occurs predominantly just interior to the standard NLR.

In addition to narrow cores, the two lowest-ionization coronal lines [S VIII] and [Si VI] show extended wings, particularly on the red side of the core. The line widths, strong flux variability on a time-scale of  $\sim$ months, and photoionization predictions all indicate that the wings are produced at a radius  $\log(R/\text{cm}) \approx 17.3$  from the nucleus. This radius is exactly coincident with the inner dust radius determined by Landt et al. (2019). We therefore associate these wings with an X-ray heated wind of material evaporating from the inner face of the torus.

This study has revealed the complex and multifaceted nature of the coronal line region in an AGN. The recent launch of the *James Webb Space Telescope (JWST)* means it is an opportune time to investigate this complexity. The high sensitivity and spectral resolution of *JWST*'s instruments will enable us to study infrared coronal lines of AGN in much greater detail.

## ACKNOWLEDGEMENTS

DK acknowledges support from the Czech Science Foundation project No. 19-05599Y, funding from the Czech Academy of Sciences via the PPLZ programme, and the receipt of a UK Science and Technology Facilities Council (STFC) studentship (ST/N50404X/1). HL acknowledges a Daphne Jackson Fellowship sponsored by the STFC. MJW acknowledges support from STFC grants ST/P000541/1 and ST/T000244/1. G.J.F. and M.D. acknowledge support from NSF (1816537, 1910687), NASA (ATP 17-ATP17-0141, 19-ATP19-0188), and STScI (HST-AR-15018 and HST-GO16196.003-A).

## DATA AVAILABILITY

The raw data underlying this work are publicly available at the NASA IRTF Archive hosted by the NASA/IPAC Infrared Science Archive (<https://irsa.ipac.caltech.edu>). The processed data are available on request from the second author.

## REFERENCES

- Appenzeller I., Oestreicher R., 1988, *AJ*, 95, 45
- Arav N. et al., 2015, *A&A*, 577, A37
- Baldwin J., Ferland G., Korista K., Verner D., 1995, *ApJ*, 455, L119
- Bohn T., Canalizo G., Veilleux S., Liu W., 2021, *ApJ*, 911, 70
- Brandt W. N., Pounds K. A., Fink H., 1995, *MNRAS*, 273, L47
- Cann J. M., Satyapal S., Abel N. P., Ricci C., Secrest N. J., Blecha L., Gliozzi M., 2018, *ApJ*, 861, 142
- Cann J. M. et al., 2021, *ApJ*, 912, L2
- Cardelli J. A., Clayton G. C., Mathis J. S., 1989, *ApJ*, 345, 245
- Cerqueira-Campos F. C., Rodríguez-Ardila A., Riffel R., Marinello M., Prieto A., Dahmer-Hahn L. G., 2021, *MNRAS*, 500, 2666
- Crenshaw D. M., Kraemer S. B., 2000, *ApJ*, 532, L101
- Crenshaw D. M. et al., 2000, *AJ*, 120, 1731
- De Robertis M. M., Osterbrock D. E., 1986, *ApJ*, 301, 727
- Dehghanian M. et al., 2019, *ApJ*, 877, 119
- Dehghanian M. et al., 2020, *ApJ*, 898, 141
- Ebrero J. et al., 2016, *A&A*, 587, A129
- Edelson R. et al., 2015, *ApJ*, 806, 129
- Erkens U., Appenzeller I., Wagner S., 1997, *A&A*, 323, 707
- Ferguson J. W., Korista K. T., Ferland G. J., 1997, *ApJS*, 110, 287
- Ferland G. J. et al., 2017, *Rev. Mex. Astron. Astrofis.*, 53, 385
- Ferrarese L., Pogge R. W., Peterson B. M., Merritt D., Wandel A., Joseph C. L., 2001, *ApJ*, 555, L79
- Filippenko A. V., Halpern J. P., 1984, *ApJ*, 285, 458
- Gardner E., Done C., 2017, *MNRAS*, 470, 3591
- Gelbord J. M., Mullany J. R., Ward M. J., 2009, *MNRAS*, 397, 172
- Giannuzzo E., Rieke G. H., Rieke M. J., 1995, *ApJ*, 446, L5
- Glidden A., Rose M., Elvis M., McDowell J., 2016, *ApJ*, 824, 34
- Grandi S. A., 1978, *ApJ*, 221, 501
- Greenhouse M. A., Grasdalen G. L., Woodward C. E., Benson J., Gehrz R. D., Rosenthal E., Skrutskie M. F., 1990, *ApJ*, 352, 307
- Grupe D., Beuermann K., Mannheim K., Bade N., Thomas H.-C., de Martino D., Schwobe A., 1995, *A&A*, 299, L5
- Hopkins P. F., Hayward C. C., Narayanan D., Hernquist L., 2012, *MNRAS*, 420, 320
- Kaasra J. S. et al., 2014, *Science*, 345, 64
- Kollatschny W., Bischoff K., Robinson E. L., Welsh W. F., Hill G. J., 2001, *A&A*, 379, 125
- Komossa S. et al., 2008, *ApJ*, 678, L13
- Komossa S. et al., 2009, *ApJ*, 701, 105
- Koski A. T., 1978, *ApJ*, 223, 56
- Landt H., Ward M. J., Steenbrugge K. C., Ferland G. J., 2015a, *MNRAS*, 449, 3795
- Landt H., Ward M. J., Steenbrugge K. C., Ferland G. J., 2015b, *MNRAS*, 454, 3688
- Landt H. et al., 2019, *MNRAS*, 489, 1572
- Mazzalay X., Rodríguez-Ardila A., Komossa S., McGregor P. J., 2013, *MNRAS*, 430, 2411
- Mehdipour M. et al., 2015, *A&A*, 575, A22
- Müller Sánchez F., Davies R. I., Eisenhauer F., Tacconi L. J., Genzel R., Sternberg A., 2006, *A&A*, 454, 481
- Müller-Sánchez F., Prieto M. A., Hicks E. K. S., Vives-Arias H., Davies R. I., Malkan M., Tacconi L. J., Genzel R., 2011, *ApJ*, 739, 69
- Murayama T., Taniguchi Y., 1998, *ApJ*, 497, L9
- Navarro J. F., 2019, in McQuinn K. B. W., Stierwalt S., eds, *Proc. IAU Symp. 344, Dwarf Galaxies: From the Deep Universe to the Present*, p. 455
- Negus J., Comerford J. M., Müller Sánchez F., Barrera-Ballesteros J. K., Drory N., Rembold S. B., Riffel R. A., 2021, *ApJ*, 920, 62
- Netzer H., 1993, *ApJ*, 411, 594
- Newville M., Stensitzki T., Allen D. B., Ingargiola A., 2014, *Astrophysics Source Code Library*, record ascl:1606.014
- Oke J. B., Sargent W. L. W., 1968, *ApJ*, 151, 807
- Oliva E., Salvati M., Moorwood A. F. M., Marconi A., 1994, *A&A*, 288, 457
- Osterbrock D. E., 1977, *ApJ*, 215, 733
- Osterbrock D. E., Ferland G. J., 2006, *Astrophysics of Gaseous Nebulae and Active Galactic Nuclei*. University Science Books, Sausalito, CA
- Pancoast A., Brewer B. J., Treu T., Park D., Barth A. J., Bentz M. C., Woo J.-H., 2014, *MNRAS*, 445, 3073
- Pei L. et al., 2017, *ApJ*, 837, 131
- Pelat D., Alloin D., Fosbury R. A. E., 1981, *MNRAS*, 195, 787
- Penston M. V., Fosbury R. A. E., Bokseberg A., Ward M. J., Wilson A. S., 1984, *MNRAS*, 208, 347
- Peterson B. M. et al., 2013, *ApJ*, 779, 109
- Pier E. A., Voit G. M., 1995, *ApJ*, 450, 628
- Porquet D., Dumont A.-M., Collin S., Mouchet M., 1999, *A&A*, 341, 58
- Prieto A., Rodríguez-Ardila A., Panda S., Marinello M., 2022, *MNRAS*, 510, 1010
- Prieto M. A., Marco O., Gallimore J., 2005, *MNRAS*, 364, L28
- Rayner J. T., Toomey D. W., Onaka P. M., Denault A. J., Stahlberger W. E., Vacca W. D., Cushing M. C., Wang S., 2003, *PASP*, 115, 362
- Riffel R., Rodríguez-Ardila A., Pastoriza M. G., 2006, *A&A*, 457, 61
- Riffel R. A., Bianchin M., Riffel R., Storchi-Bergmann T., Schönell A. J., Dahmer-Hahn L. G., Dametto N. Z., Diniz M. R., 2021, *MNRAS*, 503, 5161
- Rodríguez-Ardila A., Viegas S. M., Pastoriza M. G., Prato L., 2002, *ApJ*, 579, 214
- Rodríguez-Ardila A., Prieto M. A., Portilla J. G., Tejeiro J. M., 2011, *ApJ*, 743, 100
- Rodríguez-Ardila A., Prieto A., Panda S., Marinello M., 2020, preprint ([arXiv:2010.00075](https://arxiv.org/abs/2010.00075))
- Rose M., Elvis M., Tadhunter C. N., 2015, *MNRAS*, 448, 2900
- Schlafly E. F., Finkbeiner D. P., 2011, *ApJ*, 737, 103
- Schönell, Astor J. J., Storchi-Bergmann T., Riffel R. A., Riffel R., 2017, *MNRAS*, 464, 1771
- van Velzen S., Pasham D. R., Komossa S., Yan L., Kara E. A., 2021, *Space Sci. Rev.*, 217, 63
- Veilleux S., 1988, *AJ*, 95, 1695
- Wagner R. M., Depoy D. L., 1996, *ApJ*, 467, 860
- Wang T.-G., Zhou H.-Y., Komossa S., Wang H.-Y., Yuan W., Yang C., 2012, *ApJ*, 749, 115
- Wang T.-G., Zhou H.-Y., Wang L.-F., Lu H.-L., Xu D., 2011, *ApJ*, 740, 85
- Wildy C., Landt H., Ward M. J., Czerny B., Kynoch D., 2021, *MNRAS*, 500, 2063
- Winkler H., 2016, preprint ([arXiv:1604.04515](https://arxiv.org/abs/1604.04515))

Woodward C. E., Banerjee D. P. K., Geballe T. R., Page K. L., Starrfield S., Wagner R. M., 2021, *ApJ*, 922, L10  
 Yang C.-W., Wang T.-G., Ferland G., Yuan W., Zhou H.-Y., Jiang P., 2013, *ApJ*, 774, 46  
 York D. G. et al., 2000, *AJ*, 120, 1579

### APPENDIX A: TAKING A LOOK INTO A TYPICAL CORONAL LINE EMITTING CLOUD

Fig. A1 shows the temperature inside a coronal line emitting cloud for both unobscured (green) and obscured (red) cases. The model belongs to a cloud with a column density of  $N_{\text{H}} = 10^{23} \text{ cm}^{-2}$ , hydrogen density of  $n_{\text{H}} = 10^{7.4} \text{ cm}^{-3}$ , located at  $R = 10^{17.3} \text{ cm}$  from the source. Much of our previous work rejected clouds with temperatures greater than the  $\sim 10^5 \text{ K}$  peak in the cooling function since they produce negligible optical or IR emission. However, the large column density clouds have enough extinction to produce cooler gas near the shielded side of the cloud, so we include these for completeness. These clouds occupy the lower left quadrant of the density-radius plane shown in Fig. 13.

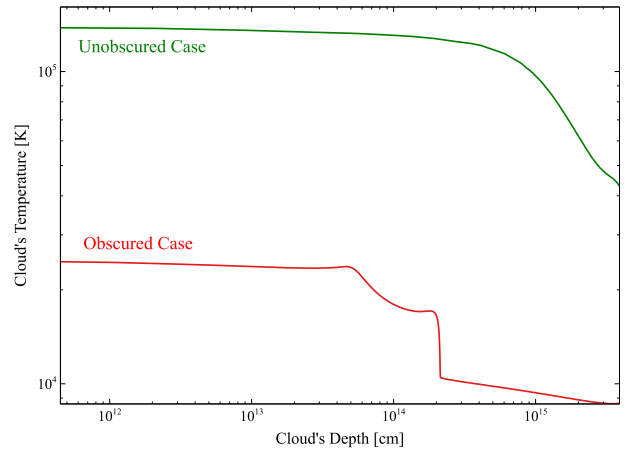


**Figure A1.** The variation of the temperature versus the depth into the coronal cloud is shown.

This paper has been typeset from a  $\text{\TeX}/\text{\LaTeX}$  file prepared by the author.